Laser powder bed fusion additive manufacturing of metals; physics, computational, and materials challenges

W. E. King' , A. T. Anderson, R. M. Ferencz, N. E. Hodge, C. Kamath, S. A. Khairallah, and A. M. Rubenchik

Citation: Appl. Phys. Rev. **2**, 041304 (2015); doi: 10.1063/1.4937809
View online: http://dx.doi.org/10.1063/1.4937809
View Table of Contents: http://aip.scitation.org/toc/are/2/4
Published by the American Institute of Physics

APPLIED PHYSICS REVIEWS **2**, 041304 (2015)

APPLIED PHYSICS REVIEWS

Laser powder bed fusion additive manufacturing of metals; physics, computational, and materials challenges

W. E. King,[1,a)] A. T. Anderson,[2] R. M. Ferencz,[2] N. E. Hodge,[2] C. Kamath,[3]
S. A. Khairallah,[2] and A. M. Rubenchik[4]
[1]*Physical and Life Sciences Directorate, Lawrence Livermore National Laboratory, Livermore, California 94550, USA*
[2]*Engineering Directorate, Lawrence Livermore National Laboratory, Livermore, California 94550, USA*
[3]*Computation Directorate, Lawrence Livermore National Laboratory, Livermore, California 94550, USA*
[4]*NIF and Photon Sciences Directorate, Lawrence Livermore National Laboratory, Livermore, California 94550, USA*

(Received 8 September 2015; accepted 3 November 2015; published online 29 December 2015)

The production of metal parts via laser powder bed fusion additive manufacturing is growing exponentially. However, the transition of this technology from production of prototypes to production of critical parts is hindered by a lack of confidence in the quality of the part. Confidence can be established via a fundamental understanding of the physics of the process. It is generally accepted that this understanding will be increasingly achieved through modeling and simulation. However, there are significant physics, computational, and materials challenges stemming from the broad range of length and time scales and temperature ranges associated with the process. In this paper, we review the current state of the art and describe the challenges that need to be met to achieve the desired fundamental understanding of the physics of the process. © *2015 AIP Publishing LLC*.
[http://dx.doi.org/10.1063/1.4937809]

TABLE OF CONTENTS

[a)] Author to whom correspondence should be addressed. Electronic mail: weking@llnl.gov

I. INTRODUCTION

A. Laser powder bed fusion

Metal additive manufacturing is "the process of joining materials to make objects from 3D computer-aided design (CAD) model data, usually layer upon layer, as opposed to subtractive manufacturing technologies."[1] Metal additive manufacturing has a number of modalities, including material extrusion, material jetting, material droplet printing, binder jetting, sheet lamination, powder bed fusion, and directed energy deposition.[2] Most current metal additive manufacturing systems are of the powder bed fusion type.[2] In the powder bed fusion process, thin layers of powder are applied to a build plate and an energy source (a laser or electron beam) is used to fuse the powder at locations specified by the model of desired geometry. When one layer is completed, a new layer of powder is applied and the process is repeated until a 3D part is produced. The powder bed fusion process is alternately known as selective laser sintering (SLS), selective laser melting (SLM), direct metal laser sintering (DMLS), direct metal laser melting (DMLM), and electron beam melting (EBM).[3] Current metal powder bed fusion additive manufacturing systems tend to use melting as opposed to sintering to build full-density parts.

Metal laser powder bed fusion additive manufacturing systems have designs similar to that illustrated in Fig. 1.[4] They are composed of powder delivery and energy delivery systems. The powder delivery system comprises a piston to supply powder, a coater to create the powder layer, and a piston that holds the fabricated part. The energy delivery system is made up of a laser (usually a single-mode continuous-wave Ytterbium fiber laser operating at 1075 nm wavelength) and a scanner system with optics that enable the delivery of a focused spot to all points of the build platform. A flow of gas (usually nitrogen or argon) passes over the powder bed with the intention to (a) protect the part from oxygen and (b) to clear any "spatter" and metal fumes that are created from the laser path. Some systems have an *in situ* process-monitoring capability that can image the melt pool using a high-speed camera or a temperature sensor that is inline with the laser system.[5]

During production, the laser executes a scanning or exposure strategy. The strategies associated with the laser path are characterized by the length, direction, and separation (hatch spacing) of neighboring scan vectors. A detailed discussion of scanning strategies is beyond the scope of this paper, but a list of scanning strategies has been compiled by Yasa.[6] Scanning strategies can affect the properties of the part including density, mechanical properties, and residual stress. Residual stress is one of several important material responses that need to be optimized for laser-based additively manufactured parts. A part can be fabricated within tolerances only to have residual stress-induced distortions put the part out of tolerance when removed from the build plate. Residual stresses can also cause a part's connection to support structures to fail or result in surface deformations that can damage the coater or inhibit the coater's motion.

B. The role of high performance computing for SLM modeling and simulation

In recent years, the state of the art in metal powder bed fusion additive manufacturing has improved to the point where it is transforming from a rapid-prototyping technology to a production technology. Parts can be fabricated at near full density (99.5+%) with mechanical properties that are similar to conventionally produced metals. Potential applications are broad, increasing, and particularly notable in the medical[2] and aerospace sectors.[7–9] Despite this progress, one of the most serious hurdles to the broad adoption of additive manufacturing of metals is the qualification of additively manufactured parts. Some 47% of manufacturers surveyed indicated that uncertain quality of the final product was a barrier to adoption of additive manufacturing.[8]

A physical understanding of the metal powder bed fusion process can provide insight into performance margins, uncertainties in those margins, and their sensitivities to process parameters. Thus, a physical understanding of the process is an essential element of part qualification. Such an understanding should also enable increased control of the process, which in turn improves the likelihood of producing qualified parts. Modeling and simulation of the additive

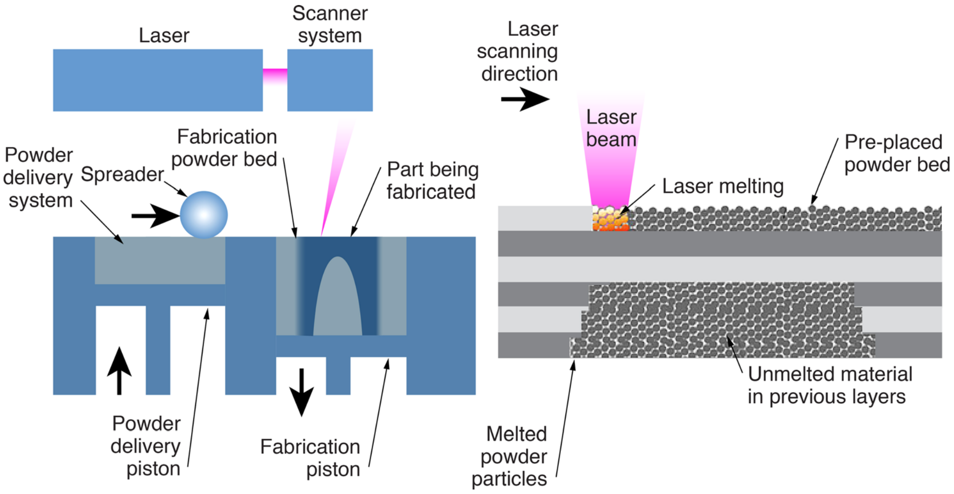

FIG. 1. This figure provides a schematic overview of the select laser melt process both at the machine and powder scales Reprinted from Knowledge Based Process Planning and Design for Additive Layer Manufacturing, KARMA, funded by the European Commission, 7th research program.[4]

manufacturing process provides a mechanism to develop this understanding. Several roadmaps for additive manufacturing have highlighted the needs for and benefits of a process modeling and simulation capability.[3,10–12] These will only be fully realized through leveraging the scale of modeling achievable through high-performance computing.

Although the powder bed fusion process is conceptually simple, the underlying physics is complex and covers a broad range of time and length scales. Laser beams and powder layer thicknesses are ∼10 s of μm and laser speeds are ∼1 m/s. On the other hand, parts are many cubic centimeters in dimension and build times can be hours, days, even weeks. Further, the process involves around 130 parameters that could affect the quality of the final part.[13] Parameters such as the laser power, speed, and beam size control the length, width, and depth of the melt pool. The geometry of the melt pool is important as its width and depth can affect part density and length can affect the microstructure through the cooling rate. Generally speaking, it is desirable to maintain a constant or controlled melt pool geometry during a build. However, because the thermal boundary conditions change as a function of the part geometry, the parameters required to achieve desired melt pool characteristics will also be a function of geometry. In current powder bed fusion systems, geometry-specific parameters can be entered for geometries such as the core, skin, and downward-facing surfaces. But, achieving controlled melt pool characteristics throughout a part requires voxel-by-voxel control of the parameters. *In situ* sensors and feedback schemes aid such control.[14–16] Feedback works best when the parameters are close to the optimal for the given geometry. This is particularly the case for the high laser speeds involved in metal powder bed fusion where the time constant for the response of the melt pool to changes in power or speed can be relatively slow. Achieving optimized input parameters is referred to as *a priori*[17] or "intelligent feed forward"[10,18] control. One system manufacturer is implementing a geometry-dependent scanning (or exposure) strategy.[19] Modeling and simulation combined with high-performance computing optimization (solving the inverse problem) have the potential to provide the next step in such voxel-by-voxel control of the process.

A number of papers have had significant impact (as measured by an average of ≥5 citations/year) in the field of modeling and simulation of the powder bed fusion additive manufacturing process. Williams and Deckard recognized the need for process modeling and simulation in the early days of polymer powder bed fusion.[20] In the case of metals, contributions with significant impact include thermal models of the process,[21–24] thermomechanical models of the process,[25,26] residual stress modeling,[27] and laser-powder interaction.[28–30]

C. Outline

In this paper, we give a brief review of recent progress in developing physics-based models for the metal powder bed fusion process. We first discuss the fundamental aspects of melting of the metal powder. We then discuss a model at the scale of the powder. This model is used to simulate the melting of powder and its resulting densification. It resolves individual powder particles in 3D. The laser-material interaction is treated via ray tracing and a physics-based absorption model. It models melting of the powder, flow and convection of the liquid, and behavior of trapped gas. It covers time scales of fractions of a second and length scales of fractions of a millimeter. We also discuss a model at the scale of the part that is used to computationally build a complete part and predict properties such as residual stress in 3D. It treats the powder as a lower-density, low-strength solid. The laser-material interaction is treated using an energy source term. The part-scale model represents melting, solidification, and includes strength; it can be readily extended to include solid-state phase transformations for future material systems of interest. It covers time scales to hours and length scales to centimeters. We discuss the role of data mining and uncertainty quantification in the modeling and simulation process and describe future applications.

II. FUNDAMENTAL ASPECTS OF MELTING

The selective laser melting process includes a variety of physical effects with huge disparities in temporal and spatial scales, making comprehensive, first-principles modeling practically impossible. However, the disparity in scales enables the use of simplified models for aspects of the process. A simulation at the scale of the powder would consider the laser interaction with the powder, powder melting, and evolution of the melt (see Section III). A simulation at the scale of the part would take into account laser heating and melting treated as a thermal source, part shape, and laser scan strategies and would be able to calculate the residual stresses (see Section IV). The ranges of applicability of the simulations can overlap, opening the possibility for the mutual code validation.

Modeling of the SLM process has some similarities with modeling of welding, but with two significant differences. First, in SLM we must be able to model the new physics associated with the interaction of the laser with the metal powder, including radiation absorption and scattering, powder melting, and melt wetting. The second is a possible significant simplification of the description. It is clear that additively manufactured material quality degrades when the energy deposited exceeds the threshold for keyhole mode melting.[31] This means that modeling of the SLM process does not need to include the plasma formation description, the radiation interaction with the vapor, and the variety of the interface instabilities that are observed in keyhole mode.

A. Numerical modeling of powder absorptivity

An important component of metal additive manufacturing process modeling efforts is the description of the absorption of laser light by the metal powder and the spatial distribution of the absorbed energy. Direct measurements of the absorption are quite difficult.[32] Also it is problematic to make use of measurements obtained without detailed specifications of the experiment, since the absorption depends on the powder material, the distribution of particle sizes, the spatial distribution of the particles, and the laser beam size and profile. Thus, it is not sufficient to know only the results for one particular powder of a given material and for a

TABLE I. Absorptivity calculated for a number of materials and material configuration (α denotes the absorptivity).

(1) Material	(2) Re(n)	(3) Im(n)	(4) α (flat surface)	(5) α (isolated sphere)	(6) α (top layer)	(7) α (bottom layer)	(8) α (substrate)	(9) α (spheres + substrate)	(10) α (spheres + substrate)/α (flat surface)
Ag	0.23	7.09	0.018	0.020	0.072	.047	0.010	0.13	7.2
Al	1.244	10.	0.047	0.056	0.15	0.063	0.011	0.22	4.7
Au	0.278	7.20	0.021	0.024	0.081	0.050	0.011	0.14	6.7
Cu	0.35	6.97	0.028	0.032	0.101	0.055	0.011	0.17	6.1
SS	3.27	4.48	0.34	0.36	0.53	0.062	0.013	0.60	1.7
Ti	3.45	4.	0.38	0.40	0.56	0.062	0.014	0.64	1.7

particular beam. Similarly, the spatial distribution of absorbed energy is difficult to obtain experimentally. These considerations reinforce the usefulness of absorption calculations.

A commonly used laser absorption model proposed by Gusarov *et al.*[33] assumes diffusive radiation transport in the powder. The model can be applicable to a ceramic powder or to a thick, high-porosity metal powder. This assumption, however, is not applicable for the thin (a few powder particles thick), low-porosity metal powder layers used in the selective laser-melting process. As we shall see, in this case most of the energy is absorbed at the surface of the top layer, and the absorption is highly non-uniform even on the scale of individual powder particles. This situation is inconsistent with a diffusion model. Also, Gusarov *et al.*[33] assume volumetric deposition of the energy instead of surface deposition. In a typical experimental situation, the diffusion time a^2/D is longer or comparable with dwell time a/u. Here, a is a powder particle size, D is material thermal diffusivity, and u is scan speed. In reality, the laser deposits the energy on the surface of the particle changing the melt dynamics in comparison with the volume deposition.

Physically, the powder is an assembly of metal particles, taken here to be spheres, with sizes appreciably larger than the laser wavelength (taken as about 1 μm) and with a complex refractive index appropriate to the material and the wavelength. It is natural to use ray tracing to calculate the powder absorption. This has previously been considered, e.g., in Wang *et al.*,[34] but the angular and polarization dependence of the absorption of incident rays was neglected.

Boley *et al.*[35] reported the results of comprehensive absorption modeling, including all the effects mentioned above. A challenge was the problem of tracing rays within an assembly of thousands of objects, while keeping track of the angle, polarization, power, and reflection/refraction of individual rays. However, this issue has long been considered, and commercial software is available for handling it. Boley *et al.*[35] used the FRED[36] code, a multipurpose optics code widely used in optical design and analysis.

To begin the calculations, we consider a powder consisting of spheres of a single size that are densely packed in a hexagonal structure. Six materials (Ag, Al, Au, Cu, stainless steel [SS], and Ti) are considered. We first study the overall absorptivity of such a powder, by assuming a uniform beam of width large compared with the particle size, so that the absorption is nearly independent of the beam position. The refractive indices near 1 μm were taken from a data compilation.[37] The results are summarized in Table I. Most important for each metal is the total absorptivity by the spheres and the substrate (column 9). This is to be compared with the absorptivity of the metal at normal incidence on a flat surface (column 4), and the average absorptivity of an isolated sphere illuminated by a uniform beam (column 5). The calculations show that the resulting powder absorptivity is significantly higher than the absorptivity of a flat surface or of a single, isolated sphere, thus confirming the important role of multiple scattering, as illustrated in Fig. 2. A ray can scatter repeatedly, leading to additional absorption relative to the case of a flat surface. Thus the relative increase in absorptivity is higher for highly reflective metals (Ag, Al, Au, and Cu) than for moderately absorbing metals (SS and Ti). In the former case, this ratio (column 10) varies from 4.7 to 7.2, while in the latter case the ratio is 1.7. Note that most of the power is absorbed in the top layer of the spheres (column 6). Little more than 1% of the power penetrates beneath the two layers to the substrate (column 8).

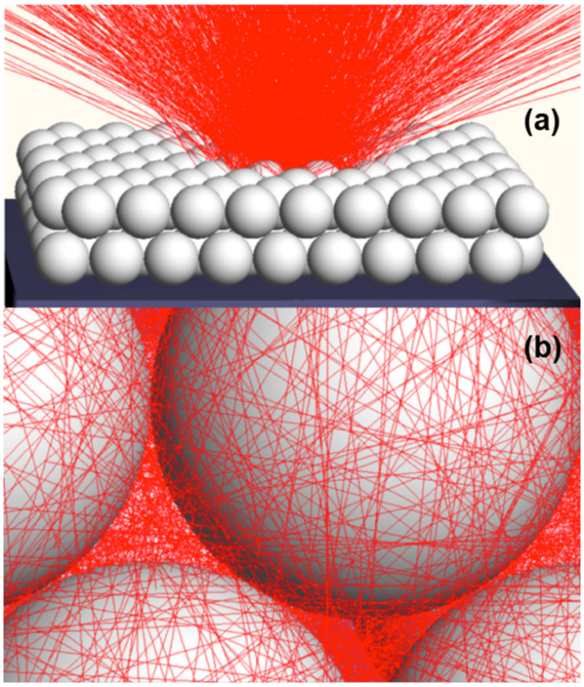

FIG. 2. (a) Typical rays during illumination of the ideal array. (b) Detail of ray trajectories in (a), showing multiple scattering from spheres.

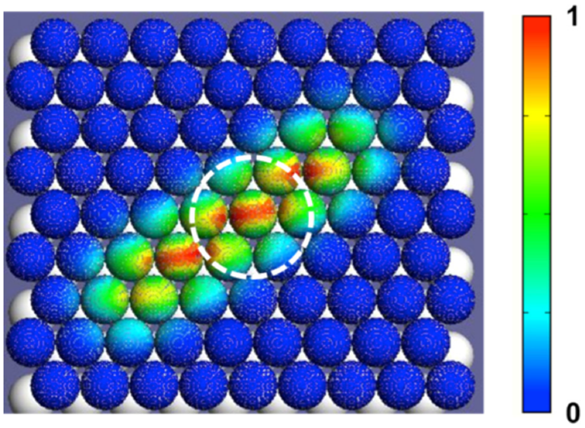

FIG. 3. Irradiances (arbitrary scale) for 61 successive beam positions, from lower left to upper right, in steps of 2 μm. The irradiances pertain to the spherical surfaces. A sample beam spot (1/e^2 radius) is shown.

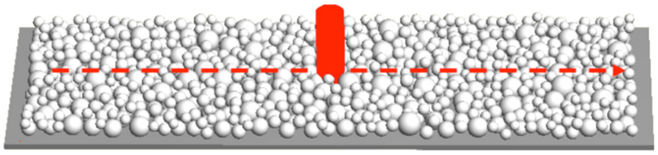

FIG. 4. Powder with a Gaussian distribution of sizes. The length of the bed is about 1100 μm, and the beam path is indicated.

More generally, one is interested in not only the total absorbed power but also the spatial distribution of the absorbed power. In some additive manufacturing machines, the laser beam size is roughly comparable to the powder particle size. Here we consider a powder with spheres of radius 10 μm and a beam having a 1/e^2 radius of 24 μm.

Fig. 3 shows the distribution of absorbed irradiance along the top layer of an array of stainless steel spheres as the beam is rapidly scanned across the array. This distribution was obtained by calculating the absorbed irradiance pattern at a number of points along the path and plotting the sum as a function of position. It gives a qualitative picture of the absorbed irradiance on a time scale short compared to thermal times, i.e., for a sufficiently fast scanning speed. We see that the scattered light is well confined and that the typical absorption area is comparable to the beam area.

The absorptivity can be sensitive to the beam size, and fluctuations of the absorptivity are smoothed with increasing beam size. For the example presented in Fig. 3, the absorptivity fluctuates along the scan by about 20% and the distribution of absorbed power in a single sphere is very non-uniform.

Real powder is different from the monosized powder considered above. A realistic powder has a distribution of sizes and a non-uniform geometrical arrangement, generally with porosity greater than that of an ideal array. To generate the powder geometry, Boley *et al.*[35] used a particle-packing algorithm[38] similar to that of the rain model for random deposition.[39] The algorithm randomly places powder particles with a specified distribution of sizes on a powder bed until the first contact with other particles or with the substrate. If the contact is with a particle, the particle is randomly perturbed, in an effort to minimize the potential energy. To simulate the removal of extra powder by a coater blade, the algorithm inserts a plane at a specified distance from the substrate and removes all particles intersected by the plane or situated above it. It should be noted that discrete element method (DEM) modeling is also being used by some investigators to understand the packing of the powder layers.[40–42]

Boley *et al.*[35] discussed two different types of powders. The first, shown in Fig. 4, mimics the powder used in the Concept Laser metal additive manufacturing machine (www.concept-laser.de/en/home.html). The powder has a Gaussian distribution of radii, with an average radius of 13.5 μm, a full width at half-maximum equal to 2.3 μm, radial

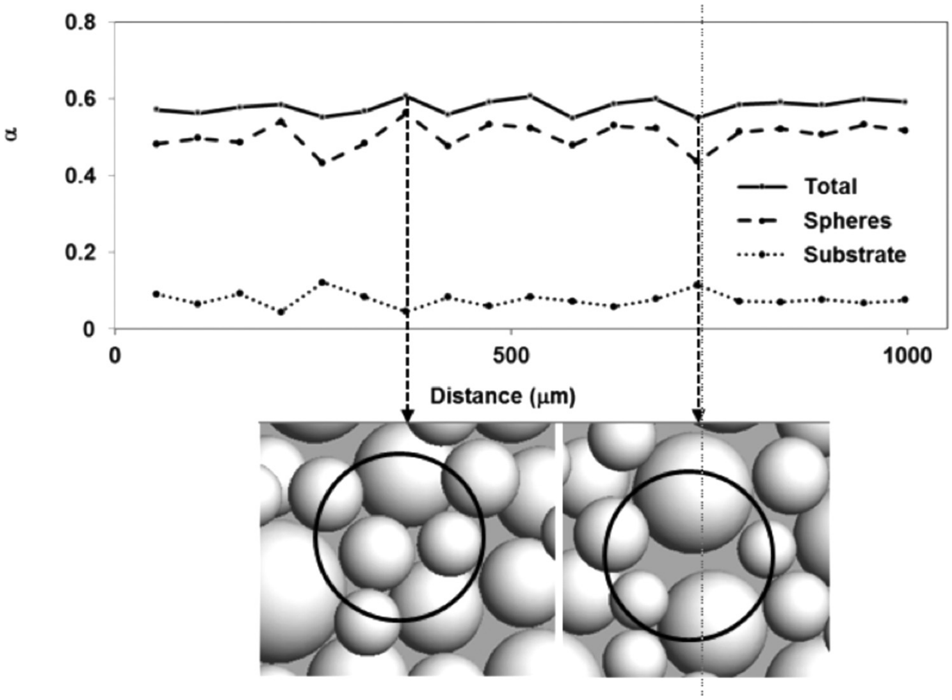

FIG. 5. Absorptivity α as calculated along the beam path for the Gaussian powder of Fig. 7. The material is stainless steel. The insets show the powder and incident beam size (1/e^2) at locations with high absorption (left) and low absorption (right).

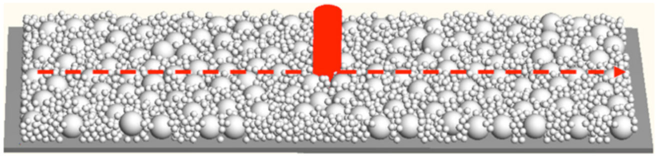

FIG. 6. Powder with a bimodal distribution of sizes. The powder bed and the beam are as in Fig. 4.

TABLE II. Total absorptivity for selected materials.

Material	Ideal array (Table I)	Gaussian array	Bimodal array
Ag	0.13	0.081	0.14
Au	0.14	0.093	0.16
SS	0.60	0.58	0.63

cutoffs at 8.5 μm and 21.5 μm, and a powder layer thickness of 43 μm.[31] In the absorption calculations, the path of the beam extends along the length of the powder bed, as shown in the figure.

The calculated absorption for stainless steel for a 1 mm laser beam path is shown in Fig. 5. Local variations in the powder structure give rise to sizeable fluctuations in the absorption. The fluctuations occur on a scale of about 100 μm, which is much larger than the typical sphere size. The mechanism for the fluctuations can be seen in the two insets in Fig. 5. In the left inset, the incident beam has mainly struck small spheres, with larger spheres on the periphery. This results in multiple reflections and an increased absorption. In the right inset, on the other hand, much of the incident power has reached the substrate, producing fewer reflections and a decreased absorption.

For the second example of a powder, shown in Fig. 6 (Ref. 35) consider a bimodal distribution characterized by a 7:1 ratio of radii and a volume fraction of small spheres equal to 20%, as discussed in Kelkar *et al.*[43] This powder was chosen because of its high density, or low porosity. Following Kelkar *et al.*[43] we consider a large-sphere radius of 42 μm and a powder thickness of 50 μm.

Fig. 7 shows the calculated absorption for stainless steel along a 1 mm laser beam path. In this configuration, holes in the powder layer are practically absent. The absorption minima correspond to situations when the beam mainly strikes a large sphere, with much of the light directly reflected (left inset). The largest absorption occurs when the beam strikes a local assembly of small spheres, as seen in the right inset. The difference between these two cases lies in the ratio of the beam size to the size of the irradiated spheres, with a larger ratio offering more opportunity for multiple reflections. As in the previous case, the absorption fluctuates on a distance scale larger than a particle size, or about 100 μm.

Parenthetically, it should be noted that the problem of a powder structure producing a maximum density has been investigated in a number of studies, e.g., see Hopkins *et al.*[44] Powder packing with density over 80% of the bulk material was demonstrated computationally for complex powder size distributions but may not be practical.

Returning to the Gaussian and bimodal powders, let us compare the overall results with those for the hexagonal powder array of Sec. II A. The results are summarized in Table II, which demonstrates that a change in the powder structure can noticeably affect the absorptivity. For a moderately absorbing metal such as stainless steel, the difference is not large, about a few percent. As a consequence, the absorptivities of the stainless steel and titanium are not very sensitive to powder structure and powder feed system. On the other hand, for highly reflective metals such as silver and gold, the variation can be nearly a factor of two. In these cases, multiple scattering is very important, and the powder configuration and size distribution affect the total absorptivity.

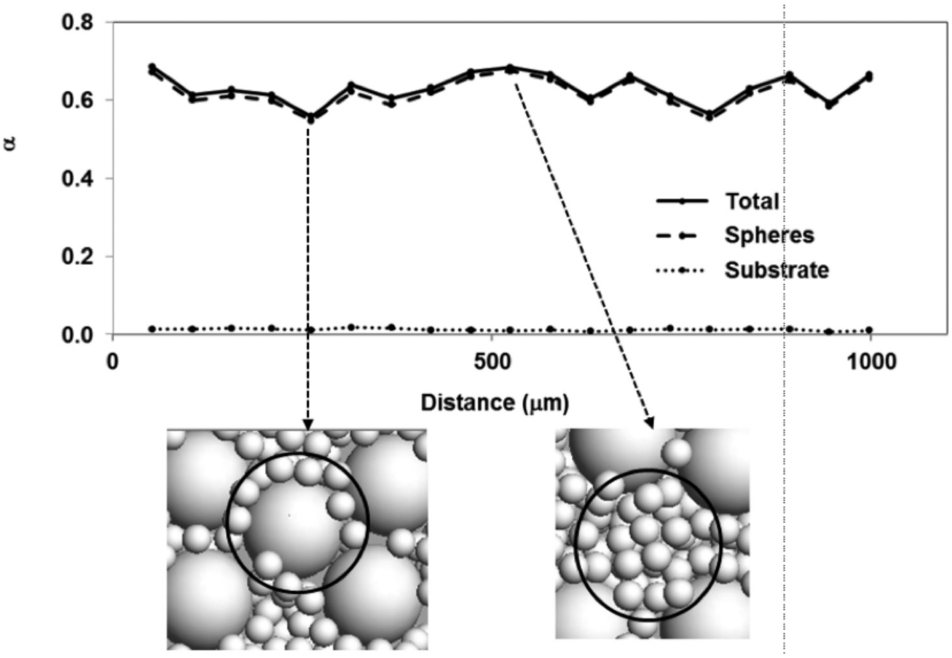

FIG. 7. Absorptivity α as calculated along the beam path for the bimodal powder of Fig. 5 (stainless steel). The insets show the powder and incident beam size at locations with low absorption (left) and high absorption (right).

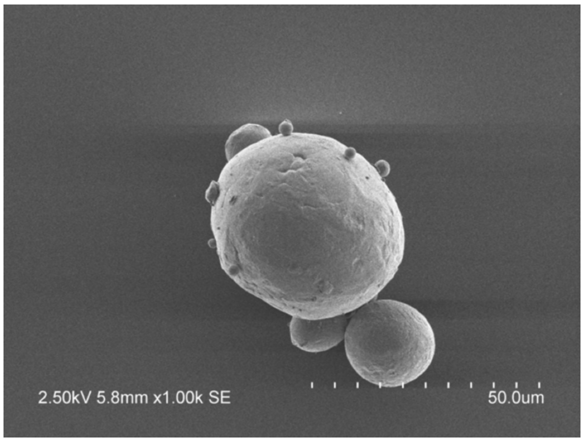

FIG. 8. Scanning electron microscope image of the real, stainless steel powder, with rough surface and agglomeration with small particles.

B. Direct absorptivity measurements

There are many reasons to do direct absorptivity measurements, even in the presence of detailed absorptivity simulations: the powder particle shape can differ from ideal spheres, (see Fig. 8), the real powder structure in an experiment can differ from that produced by the numerical model, surface oxides can affect the absorptivity, and the refractive index of the alloy materials can be very different from the pure metal measurements.[45] As an example, the Al absorptivity for 1 μm light according to Palik[37] is about 5%. The real measurements of the bulk Al gives absorptivity about 20%. This is partially explained by the effect of the oxide layer and partially by the surface roughness.[45,46]

As a result, there is increasing demand for a simple compact system for fast measurements of the temperature-dependence of the laser absorptivity up to and including the molten state. Existing systems, e.g., see Tolchko *et al.*[32] and McVey *et al.*,[47] measure the reflected light from the powder with the help of an integrating sphere and are typically complex and expensive. The distribution of the scattered light is broad and even the small absorption in the integrating sphere coating can affect the result. Calorimetry has also been used to measure the absorbed energy for a moving beam melting the powder layer. But in this case the most energy was absorbed by the melt not powder and the losses due to the radiative and convective transport were unaccounted effectively increasing the absorptivity.[48]

Recently,[49] a simple calorimetric scheme for direct absorptivity measurements had been proposed. The scheme of the measurements is presented in Fig. 9. A thin layer of powder is placed on a thin disk made from refractory metal. A laser or diode array beam uniformly irradiates the thermally isolated disk. The temperature increase is measured by thermocouples underneath the disk. The disk holder is designed such that it does not significantly absorb radiation nor affect the temperature distribution in the target. The input heating is selected to be slow compared to the rate of thermal diffusion, resulting in a uniform temperature through the powder and substrate. The temperature across the face of the disk will be uniform due to the uniform nature of the laser irradiation.

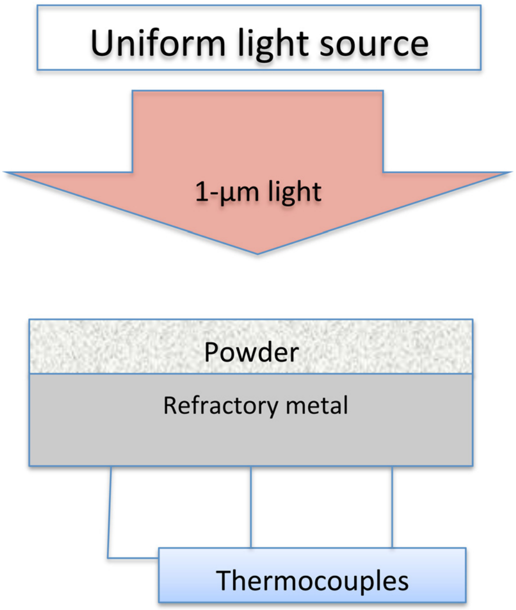

FIG. 9. Diagram of the measurement scheme. A thin layer of powder is placed on a thin disk made from refractory metal and is uniformly irradiated by 1 μm laser light sources. Temperature is measured by thermocouples attached to the bottom of the disk.

Consider a thin layer of powder with thickness d_1 on a flat disk substrate of refractory metal with thickness d_2 and radius R uniformly illuminated by light with intensity I. For absorptivity of powder (or melt), assuming uniform temperature through the disk, the temperature evolution is

$$(\rho_1 c_1 d_1 + \rho_2 c_2 d_2)\frac{dT}{dt} = A(T)I - Q(T), \qquad (1.1)$$

where $A(T)$ is the absorptivity, $Q(T)$ is the thermal losses including convective and radiative losses, ρ is the density, c is the specific heat, d is the thickness, and subscript "1" for powder and "2" the substrate.

Consider a flat top, finite duration heating pulse. A typical temperature history is presented in Fig. 10 and comprises two phases, heating and cooling. First, we consider the temperature evolution during the cooling phase, when $I = 0$ in order to determine the convective and radiative losses $Q(T)$ for known heat capacities and material densities. Next, we

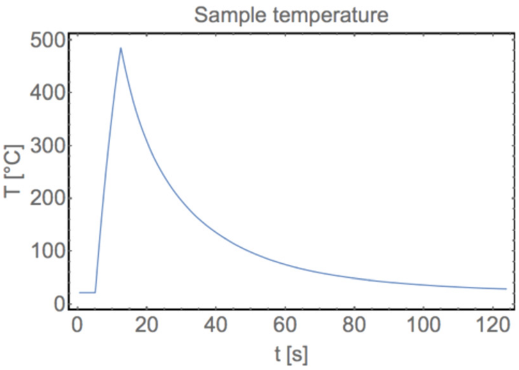

FIG. 10. Sample data from thermocouples attached to the refractory disk showing the temperature variation during the heating and cooling periods.

will find the temperature dependent absorptivity *A(T)* considering the temperature evolution during the heating phase. The missing piece in this scheme is the measurement of the powder density (porosity). This problem can be solved through a special target design. The target disk with diameter *d* has a rim with height *h* to determine the powder thickness. The disk is filled with powder and a blade or roller removes the extra material, mimicking the powder deposition of commercially available additive manufacturing systems. If we multiply Eq. (1.1) by the disk area S, the equation can be rewritten as

$$(m_1 c_1 + m_2 c_2)\frac{dT}{dt} = A(T)P - Q(T)S. \qquad (1.2)$$

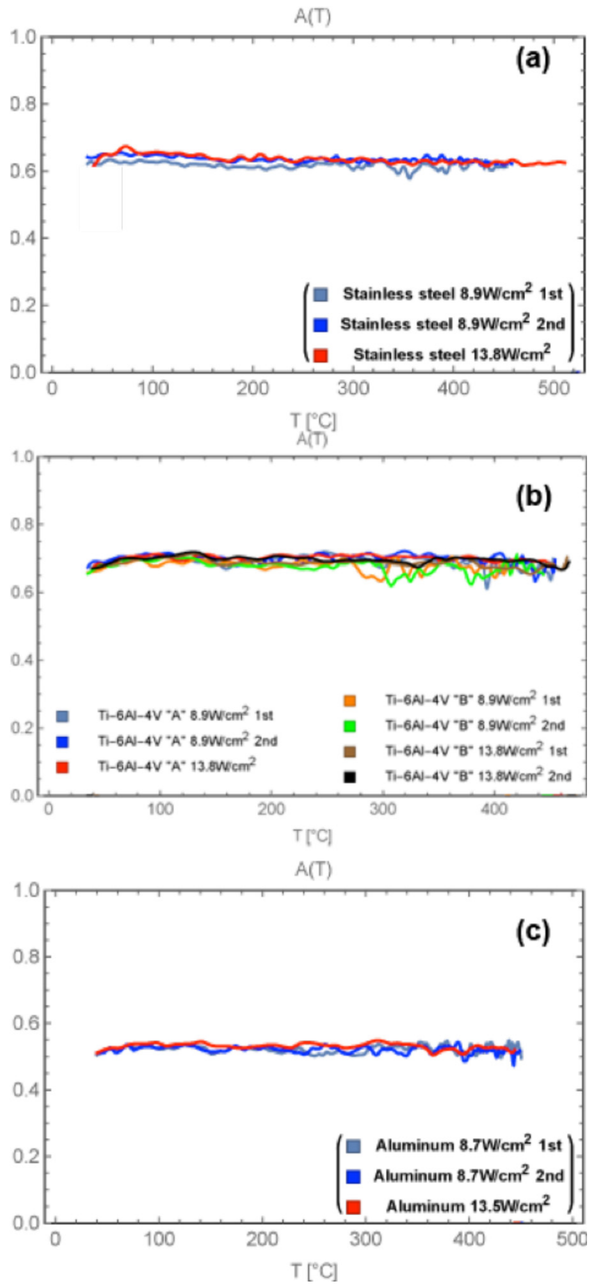

FIG. 11. Measured absorptivity data for (a) stainless steel 316L, (b) Ti-6Al-4 V, and (c) 99.9% purity Al (Goodfellow Al006031).

Here, m_1 and m_2 are the masses of the powder and disk, respectively. $P = IS$ represents the total power incident on disk. Weighing the disk with and without powder gives the powder weight needed to calculate the absorptivity from Eq. (1.2). A similar set-up was used in a previous study to measure the absorptivity of solid metal, see Rubenchik *et al.*[46] where more details of physical effects related to the experiment can be found.

Measurements[49] were done for 316L stainless steel, Ti-6Al-4V, and 99.9% purity Al powder. The density and heat capacity of Ta as function of temperature were taken from Bodryokov.[50] For stainless steel, Ti alloy, and Al, we used the density and heat capacities from Mills.[51] The results of the measurements are presented in Figs. 11(a)–11(c). The stainless steel powder (Fig. 5(a)) was the same as used in experiments carried out in a Concept Laser AM machine. The powder has a Gaussian size distribution with average radius 13.5 μm, a full width at half-maximum of 2.3 μm, radial cutoffs at 8.5 μm and 21.5 μm.[31] After the first measurement the sample was allowed to cool and the measurement was repeated (blue lines). Some small difference in results has been observed, probably due to powder re-configuration driven by thermal expansion. Performing the measurement at two laser intensities gave consistent results, suggesting that the absorptivity is independent of the heating rate.

For Ti-6Al-4V (Fig. 11(b)), measurements are from powders from two different suppliers. The powders have different particle size distributions (with the same average diameter ∼27 μm, same as for stainless steel) and they behaved differently when spread across the target disk. One powder was more cohesive than the other, tending to stick to the coater blade and roller and to form clusters. Al powder of 99.9% purity was supplied by Goodfellow (Goodfellow Al006031).

The measurements presented here were done at temperatures up to 500 °C. At higher temperatures, oxidation becomes important and the material changes color.[46] In a typical additive manufacturing process, the melting takes place in an Ar environment and we plan to make our high-temperature measurements under similar conditions. The use of a Ta disk presents a possibility to go above the melting points of most materials of interest and measure the absorptivity of the melt.

Let us compare the results with recent, first-principles modeling of laser absorption in powder using the ray tracing code presented above. It was demonstrated that due to multiple scattering the powder absorptivity is greatly increased in comparison to flat surface absorptivity. The absorption for the metals with high absorptivity (SS, Ti) is practically independent of powder structure. For stainless steel, the calculated results presented in Tables I and Table II give 60% absorptivity for monosized hexagonally packed powder and 58% for powder with experimentally measured size distributions packed according to the “rain drop” method.[38] Experimental measurements are consistent with these calculations.

The insensitivity of absorption to the powder structure may explain the independence of Ti-6Al-4V absorption on powder type. The absorptivity value for Ti alloy in our measurements is about 70%, somewhat higher than predicted by the modeling value ∼65% (Table I) One possible explanation is that the calculations in Boley *et al.*[35] used the refractive index for the pure Ti, which can differ from that of Ti-6Al-4V.

Calculated values for Al are very different from the measurements (Fig. 11(c)). They suggest that the oxide layer and the structure of the surface are important. For a flat surface, the observed absorptivity of Al is over 20% for 1 μm light, much higher than the 5% value predicted using the textbook refractive index (see discussion in Rubenchik *et al.*[46]). The increase in powder absorptivity in comparison with a solid material is consistent with numerical results.[35]

III. MODELING AT THE SCALE OF THE POWDER

A. Description and purpose

The powder scale model uses the input laser beam characteristics to transform a particle bed through the dynamics of the molten state into solidified material. The model is initialized with powder particles of the desired size distribution and layer thickness, often on a uniform substrate or on a previously processed layer. The combined thermal and hydrodynamic simulations model the appropriate distribution of the laser's energy as it interacts with the powder particles, the substrate, and the melt pool. The deposited energy from the laser heats the powder above the melting point, where the model coalesces the particles into a melt pool that flows under the influence of surface tension and vaporization recoil. The powder model tracks the various modes of heat loss, including conduction and evaporation, until the melted material solidifies onto the existing substrate. The contributions of the powder model to the overall additive manufacturing modeling effort come in four areas: laser interaction with the powder bed, powder response, melt pool characterization, and the build quality metrics of surface finish and final part density.

The total energy absorbed from the laser is an important integrated quantity that must be provided by the powder model. Another important quantity, the net energy deposited into the part, accounting for losses including evaporation and thermal radiation, will also come from the powder model simulation results. The net deposited energy plays an important role in the part scale model simulations, particularly as the details of individual layers are abstracted away for computational efficiency. The powder model has the capability to include effects of the laser beam geometry, including spot size and shape and various option for the distribution of power within the beam, such as Gaussian, top hat, or "donut."

Through modeling of various arrangements of individual powder particles, the powder scale simulations are used to determine their integrated effects. The particle size distribution is used by the powder model to initialize the geometry, thereby affecting a number of model outputs, including the powder bed packing density and the effective thermal conductivity of the unconsolidated powder bed. The thickness of the powder layer has significant effects on the part quality, including the obtainable density and surface roughness, which can be investigated with a powder scale model.

The powder model includes the formation, evolution, and eventual solidification of the melt pool. Single-track[52] parameters such as width, height, and depth can be compared with experimental data for validation of the model. The powder model can determine the uniformity of the track/bead, which is useful for creating maps of optimal process parameters. As part of the hydrothermal calculations of the melt pool motion and solidification, the powder model can generate temperature-time history data for use in models of microstructure evolution.

The role of the powder model also includes build-quality measures such as surface roughness and obtainable density. Multi-track simulations will give the solidified shape of many overlapping or overlaying melt tracks, giving the roughness of top, bottom, and side-facing surfaces of the part. These simulations can also be used to study the formation of voids in the final part structure. The powder model may be used to investigate mitigation strategies to improve these quantities by such techniques as laser power or speed variations.

B. Physics representation

1. Included physics

The powder model begins with the three-dimensional geometry of a random powder layer on a substrate. A preprocessing program generates the locations of non-overlapping spheres with the desired particle-size distribution in a randomly packed arrangement. The program fits in spheres until the desired density fraction is reached, usually near the typical experimental value of about 55%. The powder particles are overlaid on a uniform background mesh, replacing the background "void material" with metal for finite elements within the preprocessing program's defined spherical shapes. The background mesh is fine enough, typically about 3 microns, to resolve the individual powder particles.

Several approaches are possible for modeling the interaction of the laser beam with the powder bed. Some approaches (e.g., see Gusarov *et al.*[53]) utilize the methods of radiation transport to analyze the absorption and scattering of the laser beam within a 50% dense packing of uniform spheres. These methods determine an energy deposition profile that is not concentrated at the surface of the powder bed, but rather is distributed into the depth of the powder layer with a roughly exponential fall-off. The depth of deposition is determined by the packing fraction, the powder bed depth, and the absorptivity of the metal particles. This energy deposition profile is moved with the laser scanning velocity at a fixed height corresponding to the nominal powder bed depth. These methods are most applicable to applications such as SLS, where the particles for the most part retain their original geometric arrangement for the duration of the laser irradiation.

For SLM applications, the powder particles rapidly melt and begin to consolidate well within the laser beam spot, so that a more dynamic laser deposition model is required. An approach is needed that will deposit energy on the powder particles and melt surface, dynamically following the melt pool evolution. Powder scale models that include the recoil pressure from evaporation of the metal show significant depression of the melt surface under the laser beam, to below the original substrate level. Energy deposition models that provide fixed deposition versus depth profiles then have almost no metal remaining in the deposition volume.

Perhaps ideally, the laser deposition would be modeled with a ray-tracing algorithm that would operate in an integrated fashion with the calculation of the hydrodynamic motion of the melted particles. Such an approach would properly distribute the laser energy scattered between particles near the leading edge of the beam, while accounting for deposition on the melt pool surface, as well as any absorption of laser energy reflected off a dynamically changing melt pool surface. This method is computationally challenging due to the complex, rapidly changing powder and melt surface topology.

For laser deposition, we used a ray-tracing model that does not take into account the multiple reflections. For optimal processing conditions, the laser beam must melt the powder layer and some depth of substrate to provide good bonding of the new layer. When the laser interacts with the powder particles, the particles are practically thermally isolated from each other and the melting is rapid. When the laser starts to melt the substrate, the thermal conduction losses through the substrate slow down the rate of melting. In an optimal processing regime, the substrate under the laser spot will be melted to a depth comparable with the thickness of the new layer. From the above arguments it follows that in the optimal regime, the powder particles must be melted near the leading edge of the laser spot and most of the spot intersects a smooth melted surface. The results of the modeling are consistent with the above arguments. Relatively few of the incident rays would hit the metal after reflection. From this pattern it is clear that the multiple reflections play a limited role and can be disregarded.

Another effect we do not take into account is the interaction of the laser with the evaporated plume. It is usually assumed that for intensities below $100\,\mathrm{MW/cm^2}$ the laser absorption in the evaporated plume and laser-produced plasma is unimportant. For optimal processing, we want to model the laser intensity $I < 10\,\mathrm{MW/cm^2}$. While the plasma produced as a result of this interaction can be useful as the diagnostic tool, it will not affect the energy balance or the material flow.

To account for laser light reflected away from the metal surfaces, a constant absorptivity value $A = 0.3$ was adopted in calculations. This value is a conservative lower limit, e.g., the absorptivity at room temperature is $\sim$0.34 and the absorptivity of the melt is higher. The somewhat lower value is chosen to account for the decrease in the effective absorptivity of the sloped surfaces.

The powder model tracks the energy content of the metal throughout the finite element mesh. Local temperatures are derived from the energy based on the heat capacity and the latent heat of the material, which are included in a tabular equation of state (EOS). The model also computes the density changes due to thermal expansion using this same EOS. Melting of an alloy occurs over a temperature range, and not at a particular melting temperature, and this is also included in the EOS treatment. What is not included is the hydrodynamic effect of such a "mushy zone" between solidus and liquidus, where solid and liquid phases are mixed. The model instead decreases the material strength linearly from room temperature down to zero at the liquidus temperature.

One of the primary drivers for consolidation of the melted particles and subsequent motion of the melt pool is surface tension. The powder model includes an algorithm that identifies the material boundaries between the metal and background void. Based on information on the surface locations in adjoining elements, the model determines local curvature of the metal surface and applies the temperature-dependent surface tension force to the appropriate nodes. Since there is a large curvature at a "neck" where a particle first contacts an edge of the melt pool, this is a mechanism for drawing powder particles out of the bed and into the melt pool. Gravity effects are also included in the powder model, even though these are overwhelmed by the surface tension forces.

Marangoni convection is driven by the surface temperature gradient between regions of high and low temperature on the surface of the melt pool. For many materials, surface tension decreases as the temperature increases, leading to a flow away from the melt surface closest to the laser spot. Other drivers of melt-flow motion are the inflow of newly melted material and curvature-driven surface tension. The Plateau-Raleigh instability in a long, cylindrical melt bead can cause a pinching-off of some sections of the pool from others. The strong curvature of the melt pool near the laser spot draws melt flow back into this region.

Eventually the melt must solidify, so the powder model includes several modes of heat loss from the melt and heated solid. One primary loss mechanism is through thermal conduction, largely to the substrate. This energy loss is computed as part of the thermo-mechanical solution at every time step of the simulation. The model also includes conduction through the adjacent powder bed, though this effect is limited by the poor effective thermal conductivity of the bed, only about an order of magnitude higher than the gas used as the backfill atmosphere.[54] The model uses a boundary condition on the bottom of the substrate that approximates the response of a semi-infinite slab, reducing the thickness of substrate that must be modeled. A thermal radiation loss is also computed for the top surface of the melt pool, based on the usual T^4 relation, modified by an effective emissivity of the liquid metal. The model also includes an energy loss due to evaporation, which will be discussed below.

As the melt cools, its motion is eventually stopped by the strength terms in the material model turning back on when the temperature falls below the melt temperature. As the material solidifies, the temperature and thermal shrinkage are tracked as the energy is brought lower through the thermal loss mechanisms discussed. Again, no "mushy zone" is accounted for as the material passes from liquidus to solidus.

2. Abstracted physics

Evaporation of metal, particularly under the intense laser spot, is an important part of the dynamics and energy balance of the SLM process. Because the mass loss is expected to be small and the processes are dominated by very near-surface effects, the evaporated material is not modeled directly. The powder model does include the effects of evaporation through an abstracted model approach. The two effects that are modeled are the energy loss due to the loss of metal vapor from the modeled system, and the recoil pressure that balances the momentum of the departing vapor.

The theory of rapid vaporization is well established in the literature.[55–57] Adjacent to the surface there develops a thin layer where the vapor velocity distribution is dominated by the evaporating material, and so is not in translational equilibrium. Within a few mean-free paths, collisions between the vapor molecules establish equilibrium conditions. The gas dynamics model of this thin Knudsen layer employs jump conditions that conserve mass, momentum, and energy.

There are several different treatments for the evaporation rate that boil down to the same exponential dependence on the surface temperature. For example, in Klassen[58] the Clausius-Claperon relation can be used to compute the saturation vapor pressure from the material's latent heat of vaporization, boiling temperature at atmospheric pressure, and the critical temperature. The net mass transport rate, including the effects of condensation, is computed from a local Mach number based on the ambient pressure and the saturation vapor pressure as a function of surface temperature. This result determines the evaporation coefficient, the net fraction of molecules leaving the surface. Finally, the recoil pressure is computed based on a pressure balance across the Knudsen layer using the evaporation coefficient and the saturation vapor pressure.

The powder model makes use of the recoil pressure following the treatment of Anisimov.[59] A table of recoil pressure as a function of surface temperature for a particular material is first created. The model reconstructs the location of the top surface of the melt pool every cycle using information on the volume fraction of metal in each zone and its neighbors, as discussed above in relation to application of surface tension forces. The recoil pressure forces are added normal to the local interface direction, with a magnitude determined by the local surface temperature.

The mass lost to evaporation is expected to be small, at least for the optimized build conditions for a particular material. Approximately, the mass loss is less than a percent of a single powder particle per millimeter of laser beam travel, so the powder model does not adjust masses to account for the net vaporization rate. However, the energy content of the vaporized material is significant, since the latent heat of vaporization is quite large. Using the computed net vapor flux and the latent heat of vaporization, a table is constructed giving the energy loss rate as a function of surface temperature for the material under study. The thermal solver part of the powder model uses this table as a (negative) source term applied to the surface elements of the melt pool. One great benefit of applying this evaporative cooling to the simulation is to effectively limit the peak temperature under the laser spot to near the boiling point. For example, a calculation of a 400 W laser beam on steel would give a peak temperature near 3000 K, not the 7000 K that is seen without the evaporative loss.

An underlying assumption in this evaporation treatment is that the material is pure, or can be effectively modeled with an averaged set of material properties in the case of alloys. It is well known in the laser welding literature that lower vapor pressure constituents can preferentially vaporize, depleting the remaining material in these components. The effect of our approximation is unknown, and will vary by material and processing conditions.

3. Neglected physics

One of the limits of this powder model is that it cannot be used under conditions of intense vaporization, such as those that might be found in keyhole welding.[60] The powder model assumes that there is no interaction of the vaporized material with the incoming laser beam. Doing so would involve computations of laser-plasma interactions and the subsequent re-radiation of energy deposited in the plasma back to the workpiece. While models for these processes are available in the literature, experimental evidence related to our work has indicated that a mode of SLM processing that approaches the keyhole regime is not advantageous to build quality.[60,61]

Another laser-related feature not included in the powder model is a true laser ray-tracing capability. Such a model would be expected to improve calculations of the spatial distribution of the laser energy deposition. This would particularly be true with strongly concave melt pool surfaces where reflected laser light might deposit energy on the far side of the depression, rather than being lost. Until this capability is fully installed and tested with the powder model, the line-of-sight laser deposition model will be used, albeit with some needed experimental calibration for total absorbed fraction.

The convective losses to a flowing guard gas in the build chamber are ignored in the current model. Computational limitations, discussed below, permit only small spatial areas to be modeled, on the order of a fraction of a square millimeter over a few dozen milliseconds. During these time scales, evaporation, thermal radiation, and conduction to the substrate dominate the heat loss from the solidifying melt track. The convective losses will be more important when we can scale up to several square millimeters of build area.

The current powder model ignores the gas dynamics of any trapped background gas, instead modeling only the metal and a "void material." The void disappears if a gap between two powder particles is closed, obviating the need to track the motion of any gas. The strong dynamics of the melt flow driven by Marangoni convection and the recoil pressure suggest that the melt is fairly well mixed, so any trapped gas should be able to escape, given sufficient melt depths.

The powder particles used thus far in the modeling have been spherical. The pre-processing program can utilize ellipsoids as well as spheres, but this work has not yet been done.

A more significant omission in the powder particles is ignoring any oxide layers. Although particles tend to melt fairly quickly and so change the surface, the melt flow is largely driven by surface tension. Surface tension can be significantly changed by contamination, but there tends not to be sufficient data to permit addressing this issue.

The powder model does not contain any consideration for the formation of metal grains and for grain growth as the melt pool solidifies. A simple isotropic model adds material strength as it cools below the melt temperature.

C. Computational challenges

1. Need to approximate some physics

Evaporation is an important phenomenon in SLM, but the dominant length scale is the Knudsen layer, which is much smaller than what can be explicitly modeled with the powder-scale finite element mesh. This situation demands a sub-scale model of the process that must be pre-computed by a separate model of the Knudsen layer flow. Although somewhat cumbersome, the approach of applying pre-generated tables to the simulations is quite effective.

The most significant approximation with the laser deposition portion of the powder model is the assumption of no interaction of the incoming laser with any vaporized material. With this assumption, the computational model does not need to track laser energy absorption, scattering, and subsequent re-emission. The first two factors would involve much more sophisticated laser-plasma interaction capabilities, while the last factor would require dynamically changing energy fluxes on the neighboring surfaces of the melt pool and powder bed. We are working on validation experiments to determine if this assumption is valid for the preferred range of SLM operating parameters.

2. Need for fine zoning

The powder model needs to resolve the individual particles in the powder bed. There must be adequate resolution for accurate determination of surface shapes for the surface tension computations. For the thermal solution steps, the cavities between the powder particles must be resolved to obtain an accurate model for the thermal conduction through the unconsolidated powder bed. On a coarse mesh, adjacent particles will appear to have a "neck" of connected metal between them, greatly increasing the effective thermal conductivity. These requirements have led to a typical finite element size of about 3 μm on a side, for simulating particles of a 27 μm mean diameter.

3. Explicit time marching limits time step

The powder model uses an explicit hydrodynamic formulation for the motion of the powder and the melt. This approach brings with it a limit on stability based on the time required for a sound wave to cross a zone. With a 3 μm zone size and sound speeds of a typical metal, the time-step size cannot exceed about a nanosecond. Thus simulations covering several milliseconds require millions of time steps, leading to long simulation times for detailed models.

One well-known trick to mitigate the effects of this stability restriction is to artificially raise the density of the material under study, thereby reducing the sound speed somewhat, and so increasing the minimum time step. The difficulty with this trick is that the dynamics of the material motion can be affected by this artificial density change. Through various numerical experiments using various levels of density scaling, it was found that at most a factor of three to five in sound speed could be achieved with this approach without adversely affecting the results.

D. Materials challenges

1. Experimental data required

Powder morphology is needed to properly initialize simulations of powder bed SLM, as these characteristics affect packing density and minimum reasonable powder layer thicknesses. A primary metric needed from the supplier or preferably from direct measurements is the particle size distribution. Direct measurement is important if the excess powder from previous builds is to be reused, since the particle size distribution will evolve through reuse cycles. Another metric of powder morphology is the particle shape. Spheres are of course easiest to model, but any powder with a significant amount of non-spherical particles should have some quantitative measure of the shape to ensure good fidelity in establishing the initial powder bed for a simulation. The effective packing density should be measured in the SLM machine by performing a build of a known-size box that is removed from the build chamber with the enclosed unconsolidated powder still in place. Weight measurements before and after removing this powder will provide a good target for the modeled powder bed. Our measurements have shown approximately a 55% packing fraction. This number should probably be treated as an upper bound as the powder layer becomes thin, nearing the maximum particle size.

The powder model has fairly extensive requirements for material property data. The elemental composition of the powder particles must be known, both for the main constituents and for any oxides or other impurities that might be present. Knowledge of the composition is necessary both to select the proper literature values of any properties that will not be measured, and to allow construction of tabular equations of state to cover the thermodynamic phase space. Density of the material, not just at room temperature, but as a function of temperature up to and beyond the melting point, is required for proper computation of thermal expansion. The melting temperature or solidus and liquidus temperatures for alloys must be known. The latent heat of melting must be known to properly capture the melting rate and particularly the cooling rates as the melt pool solidifies. Because evaporation of the metal can occur under the laser spot, the boiling temperature and heat of vaporization must be known for the material. For alloys, this can be an average of the properties of the constituents, or just the values for the major component, depending on the available data. The heat capacity and thermal conductivity of the material must be known from room temperature up to and beyond melt. Because much of the dynamics is driven by surface tension, this must be known for the liquid metal. To include the effects of Marangoni convection, the temperature dependence of the surface tension must also be measured. Some measure of the viscosity of the liquid metal should be made, though since many metals have rather low viscosities; however, this quantity is not as critical for success of the model. Laser absorption properties of the material must be known, both for a packed powder bed and for a solid and a liquid surface.

The laser input parameters must be known for input into the powder model. The laser wavelength is needed to properly assess absorption properties. The laser temporal characteristics must be known, either CW (steady continuous wave) or pulsed duration and repetition rate. The total power must be specified. The beam size is an important measure, and must be accompanied by a good definition of "beam size," be it 1/e^2, D4σ, 95% power, or another measurement standard. The power distribution within the laser must be specified, usually Gaussian, though flat top, donut, and other options are possible.

2. Description of material models

The powder model is based on the ALE3D multiphysics code to model the heat transfer and material motion. The thermal solution makes use of the temperature dependent thermal conductivity and heat capacity entered as part of the material data. Thermal expansion and response to pressure loading is handled using a tabular equation of state that defines pressure and temperature as functions of density and energy over the range from room temperature to boiling. The strength model is of less importance to the powder model than to the effective medium model, since the primary use of strength is to compute residual stresses in the part scale model. A standard ALE3D model of a high-deformation rate, temperature-dependent strength is used for the simulations.[62]

E. Application examples

1. Powder bed thermal conductivity

The thermal conductivity of the particle powder bed is computed "on the fly" from first principles. All that is required is the thermal conductivities of the stainless steel material and of air at a given temperature. The powder has lower thermal conductivity than bulk stainless steel. This is because the particles are at point contact and the heat diffusion in gaps between the particles depends strongly on the gas's thermal conductivity, which is lower than that of the metal.[54] As a code validation test, we compute the thermal conductivity of stainless steel powder. We find for a powder packing density of 36%, the ratio of powder thermal conductivity over thermal conductivity of air is 3.0; for 45% it is 4.2; for 55% it is 6.6. These results agree well with the values 3.0, 4.5, and 6.0, respectively, in Fig. 5 of Rombouts *et al*.[54]

2. Single track formation

First, we examine a single track simulation to illustrate the effects of melt flow driven by surface tension, including flow instabilities leading to non-uniformity of the final solidified bead. The material is stainless steel, 316L, in a powder with a log-normal distribution about 27 μm. The powder is distributed in a random packing to a depth of 35 μm on a thicker substrate. The laser source is about 1 μm wavelength, 200 W power, 2.0 m/s scanning speed, and beam size (D4σ) of 54 μm diameter. The computational domain is 1000 μm long and 300 μm wide. The simulation includes the effects of surface tension and Marangoni convection, but neglects evaporation and recoil pressure for this case.

We find that the surface-tension effects on topology and heat transfer drive the SLM process. As soon as a melt forms, the surface tension acts to decrease the surface energy. Although the viscosity is low, we still consider it whenever surface tension is computed. The model includes gravity; however, surface tension forces are stronger and the time scales we consider are short, so we do not expect gravity to play a major role.

Our fine-scale approach demonstrates the 3D nature of the SLM process and the influence of the stochastic powder bed. Figs. 12 and 13 show the temperature contour lines on the surface of the stochastic powder bed and inside the substrate, respectively. The black contours surround a region of temperatures higher than 5000 K (this temperature exceeds the boiling point and is addressed below), which indicates the location of the laser spot. The next interesting contour line is the red melt line with a temperature of 1700 K, which surrounds regions of liquid metal. One notices that the red line, i.e., liquid melt, races ahead of the laser spot. The region that separates the laser spot and the solid particles ahead is quite narrow. These contour lines also indicate that temperature gradients are the strongest near the laser spot and decrease in the back of the flow. This suggests that the Marangoni effect should contribute to the flow and that its effect will be largest close to the laser spot.

One also notices islands of liquid regions at the back of the flow (Fig. 12). The temperature profiles on the surface and the substrate are intimately connected to the melt topology. These island formations are evidence of the Plateau-Rayleigh instability, which creates peaks and troughs. At the troughs, the melt height is low. It takes less time for the substrate to cool these regions since less liquid is present there. At the peaks, the opposite is true. More liquid means more stored heat and the liquid lives longer. This non-uniformity

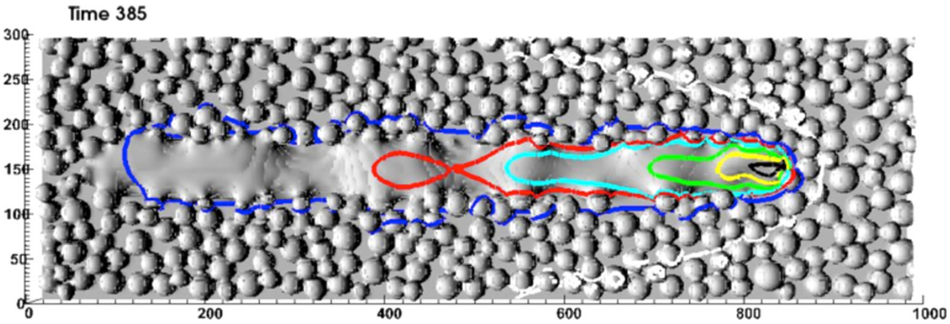

FIG. 12. 3D simulation snapshot shows the temperature distribution on the surface as the laser spot moves to the right. The time is expressed in microseconds, length in micrometers and the temperature is in Kelvin. The temperature profiles are correlated with the surface topology.

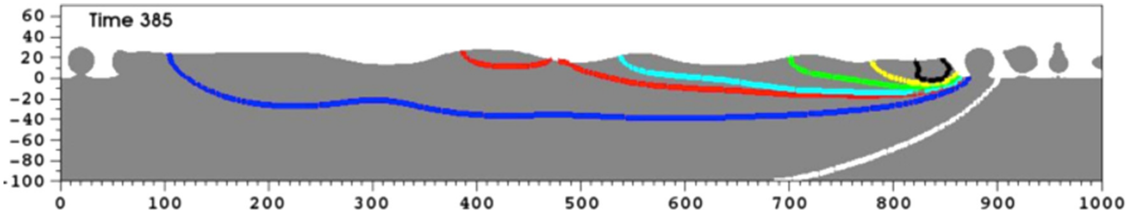

FIG. 13. This 2D longitudinal slice corresponds to the 3D snapshot in Fig. 12. The slice is taken in the middle of the melt track. It shows the temperature distribution in the melt pool and substrate. The time is expressed in microseconds, length in micrometers and temperature in Kelvin. The temperature profiles are correlated with the surface topology.

of surface cooling can be an important feature that the powder scale model can pass on to the microstructure and part scale models.

Going beyond what was shown in the previous simulation, the inclusion of recoil pressure in the powder model reveals robust dynamics under the laser spot. Fig. 14 illustrates the melt pool dynamics in a slice taken through the center of the laser path, with color indicating temperature and vectors representing the velocity field. Hot droplets are seen ejected from the melt pool, like the sparking that is observed experimentally. Spatter of liquid droplets is observed in front of the laser spot. Recoil pressure has a significant effect on the topology of the powder and melt, allowing melt penetration well into the solid substrate. Marangoni convection is moving the surface of the melt away from the laser, but the curvature of the melt surface is strongly pulling the melt back into the depression formed by the laser beam. Though not shown in the figure, inclusion of the evaporative energy loss term decreases the peak temperatures under the laser spot from being in excess of 5000 K previously to about 2700–3000 K, the boiling point of steel.

F. Alternate approaches

1. Lattice-Boltzmann methods in 2D

Granular or fine fine-scale models are expected to be computationally demanding. In Klassen[58] and Körner,[63,64] a mesoscopic simulation of the melting process uses the two-dimensional lattice Boltzmann method to create a process map. These researchers have included much of the same physics included in the present study, adding more features over time, such as the recent addition of recoil pressure and evaporative losses. These works show the influence of surface tension and the packing density of the powder bed have a significant effect on the melt pool characteristics. The process maps show regions in scan speed/laser energy space where certain melt bead morphologies are to be expected. While two-dimensional models are computationally efficient, the SLM process is inherently three-dimensional, requiring the method to employ several approximations to achieve useable results.

2. Open source models in 3D

Another recent approach applies the computational fluid dynamics toolbox called OpenFOAM, with some special-purpose routines for SLM, to model the powder bed in three dimensions.[65] The simulations presented in the paper show a uniformly packed powder bed, which reduces the stochastic nature of the powder scale processes somewhat. Their flow is driven by surface tension, though Marangoni convection was not included. The model also includes effects of evaporation under the laser beam, resulting in melt surface depression under the laser spot, in general agreement with the

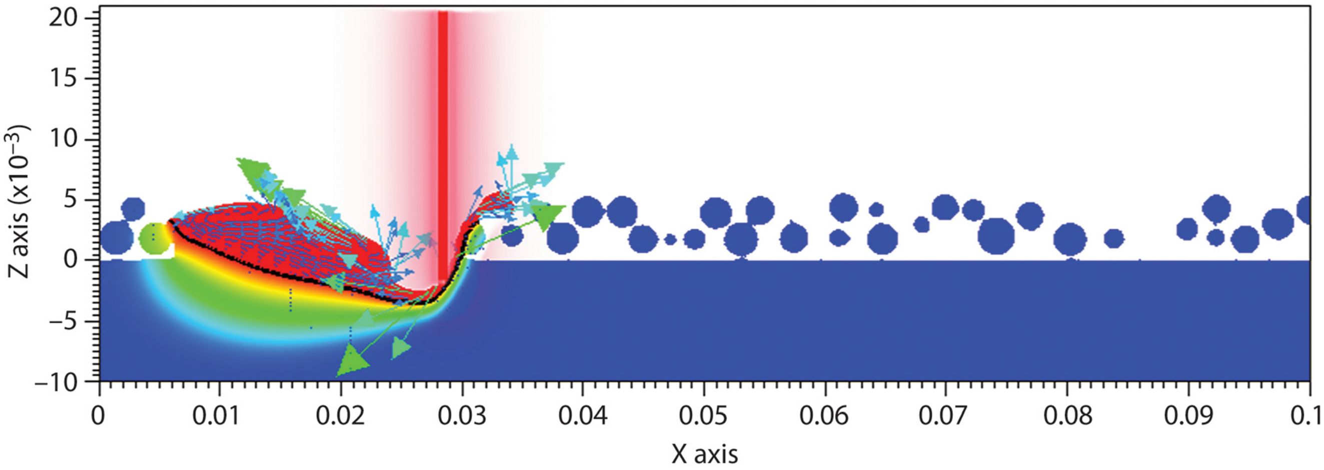

FIG. 14. This 2D longitudinal slice is taken in the middle of the melt track. Colors indicate the temperature distribution in the melt pool and substrate, with red being melted material, while the vectors represent melt velocities. The drawn-in laser beam is approximately in the correct location at this time in the simulation. The "floating" powder particles result from the 2D slice through a random 3D distribution.

present model. A primary disadvantage of their approach is that while the open-source tool is designed to be flexible, it is not well suited to large-scale calculations requiring good parallel scaling for many thousands of processor-hours.

3. Discrete element methods in 3D

The DEM is a natural choice for modeling behavior of particle beds. Some recent work in this area[66] utilizes the DEM method to analyze the selective laser sintering process, in which particles are heated sufficiently to begin to sinter together, but do not develop into a convecting melt pool. The DEM method is capable of thermo-mechanical analyses, with some calibrations required for certain parts of the model. The initial conditions in a random powder bed are set by allowing a number of particles to settle on a flat plate under the influence of gravity. For the thermal conduction, the model handles conduction between particles at contact points but must be adjusted to account for the additional gas phase conduction that is usually significant. Ganeriwala *et al*. describe the thermal solution to the laser energy deposition on the layer and the effects of particle size on melt rates. The DEM has promise for selective laser sintering simulations, but selective laser melting modeling requiring melt pool dynamics is problematic.

IV. MODELING AT THE SCALE OF THE PART

A. Purpose

The metal additive manufacturing enterprise needs information and knowledge at the overall scale of the desired part and builds process to inform many engineering decisions. Currently, these decisions are primarily informed by past experience and test fabrications. Ideally, simulation insights would help inform design, process specification and qualification, process monitoring, and part acceptance. Quantities of interest at the part scale include:

- Deformations that could halt machine operation or place the completed part outside the desired geometric tolerances
- Residual stresses causing those deformations and/or creating initial conditions detrimental to service-life concerns such as failure and fatigue
- Local effective material properties, or at least indicators of where they might significantly deviate from the nominal properties expected from the process

The ability to reliably predict such responses would aid adoption of AM technology and speed its ongoing adaptation to new material systems and specific part geometries. These predictions must be attainable in a timely manner with acceptable and assessable computational resources. An eventual goal is fabrication models that are so efficient they could be evaluated as part of the performance evaluation for a trial design within an automated design optimization process.

B. Physics challenges

Selective Laser Melting (SLM) is a process calling for multiscale modeling: local ($O(10\text{–}100\,\mu\text{m})$) extreme material transformation is taking place over brief time intervals $O(10\,\text{ms})$ as an overall part $O(10\,\text{cm})^3$ is fabricated in a processes lasting O(hours-days). Yet, in-line multiscale material response modeling is little utilized in any application space, let alone AM, due to its extreme computational demands. The very separation of these scales suggests that multiple models can each provide useful insights and build knowledge leading toward eventual coupling or coordination. In creating tractable simulation approaches for part-scale fabrication, a series of modeling topics must be addressed—or consciously avoided. The eventual strategy decisions must be tested through assessing the ability of the resulting overall model to produce meaningful insights.

The local SLM process is an extreme, thermally driven material transformation, as illustrated in Sec. III on modeling at the powder scale. At the part scale, one seeks to obscure the details of the local power-laser interaction. Instead, the goal is to capture the aggregate influence of the SLM process on the macroscopic state of the part during and at the completion of its fabrication. By choosing to ignore flow dynamics in the melt pool, the simulation can be cast as the thermo-mechanical response of a nonlinear solid continuum. Within that perspective, the powder can be represented as a reduced-density, low-strength solid. The deposition of the laser energy into the powder can then be represented by a volumetric energy source term. The spatial distribution derived by Gusarov *et al*.[67] has been one common choice, even if utilized outside the original assumptions of that analysis. Gusarov introduces a simple knockdown factor to the total nominal laser power to acknowledge the effects of reflected radiation and metal evaporation. Melting can be represented thermally through a latent heat and mechanically as a near-total loss of strength. Some researchers view the only relevant response being the subsequent freezing and choose to simply initialize the active fabrication area at T_{solidus}, e.g., Zaeh *et al*.[68] Having the temperature-dependent strength rise as temperature falls below T_{solidus} is currently our only acknowledgement of the complex behavior in the "mushy zone" at the melt pool boundary.

With an effective medium model such as discussed here, the geometry of powder particles is *not* resolved. It is indeed a choice as to what powder volume is directly represented in the computational domain. For true part-scale spatial domains, the common modeling practice to date is to largely ignore the adjacent regions of un-melted powder, at most perhaps representing their thermal interaction with the part through some Neumann boundary condition. Some of the present authors have analyzed Representative Volume Element domains consisting of a cubic millimeter of material.[69] In this case, successive $50\,\mu$m layers of powder are initialized and scanned by moving the energy source location. To model the gross loss of porosity due to powder melting, an irreversible "phase strain" was introduced into the thermo-mechanical constitutive model that is activated during the material's first excursion above T_{solidus}. This "phase strain" magnitude was simply assigned to result in a net volume associated with full-density material. If future powder-scale modeling can identify a phenomenological evolution law for porosity, e.g., based upon the local history of temperature and temperature gradients, then the part scale model could adaptively assign the appropriate local phase strain or at least output a map of regions likely to have unacceptable porosity.

C. Computational challenges

The computational challenges of part scale thermo-mechanical simulations are driven by the disparate spatial scales of the laser energy source and the overall part geometry and compounded by the disparate time scales of local heating versus overall heat transfer and the actual time of fabrication, which is at least hours and often days. This has led most researchers to concentrate on coarse mesh representations capable of capturing overall part deformations while minimizing computational costs for each time step. Others are complementing this with multi-resolution approaches, e.g., adaptive mesh refinement or forms of embedded grid, to localize some higher resolution in the vicinity of the active material transformation.

The aggregation of process representation to more computationally tractable length scales reinforces the similarities between SLM and welding: this potentially obviates some of the physical differences already noted between the two. Not surprisingly then, some of the active AM researchers come out of the weld modeling community and are informed by the well-established methodologies represented by standard texts in that field, e.g., Goldak[70] and Lindgren.[71] This is particularly so with the related metal AM technology of L Engineered Net Shaping (LENS) and similar direct metal deposition methods having a larger (wider) active deposition zone, closer to a weld bead. Representative of work in this vein are publications by Michaleris and co-workers, e.g., Michaleris *et al.*[72] and Denlinger *et al.*[73]

One approach to thermo-mechanical modeling of SLM fabrication is being pursued in the context of the computational perspective and resources at a national laboratory. Some of the present authors are involved in adapting the in-house, general purpose implicit nonlinear finite element code Diablo,[74] capable of effectively utilizing commodity parallel-processing platforms. Early efforts focused on developing SLM modeling and algorithmic approaches in the context of 50 μm layer-resolved simulations for representative volumes comprising 1 mm^3.[69] That paper provides a detailed description of the balance laws, boundary conditions and material models utilized. These coupled thermo-mechanical simulations utilize the laser deposition model of Gusarov directed in a serpentine pattern with alternating layer orientations. These calculations typically used 32–128 processors simultaneously, eventually taking less than two days. Peak heating and cooling rates of O(10^5 K) are observed, as also reported in Schilp *et al.*[75] Importantly, these simulations highlight that it is misleading to think merely in terms of the temperature history of the material in the active powder layer. These simulations clearly show that the material located several or more layers below the active work surface is still undergoing significant temperature excursions, which will contribute to continued evolution of the local microstructure.

D. Material challenges

With our current thermo-mechanical modeling strategy, the material response is represented via rather standard heat conduction and J_2-plasticity models, parameterized with temperature-dependent properties. As engineering materials are typically not envisioned to have service life at temperatures near T_{solidus}, it is not surprising that scant handbook-type property data is available in that regime. Thus, to date we have relied upon artful interpolations between available elevated temperature properties and melt. The casting literature is another area for us to explore, though the time scale of SLM solidification may not match well with useful representations/correlations established in that field of modeling. Of course none of the thermo-mechanical responses described says anything about microstructure evolution and resulting service-temperature properties. We envision role of part-scale modeling to be producing histories of temperature, temperature gradients, cooling rates, etc., that would inform a microstructure prediction model.

E. Application examples

We first consider a case where even looking at the limited domain of a representative volume provides insight into a common SLM challenge: fabrication of downward-facing surfaces. Such "overhang" features often result in an undesirable finish on the underside that could necessitate further machining—if accessible. Fig. 15 contrasts two build strategies. A common domain is defined: a 1 mm^2 plan form starting on a build plate shown in grey. For the first six layers, the energy source only scans over the left half. Blue represents unconsolidated powder and red fully transformed material; intermediate colors represent incompletely consolidated material. Starting with the seventh layer, the energy source scans the entire plan form. With the leftward case, which maintains constant laser power, we see the relative insulating properties of powder lead to localization of the energy and deeper penetration of the melt pool. With the rightward case, the laser power is modulated to one-fourth its nominal value as it reaches the right edge of the domain. This produces a transformed overhang region much nearer the desired horizontal surface. Note however this simulation also shows the mitigation strategy should only be utilized during the initial overhang layers. By the third overhang layer, the reduced power is leading to substantially incomplete melting of the powder as evidenced by the green regions.

Our modeling approach is being revised and extended to address dimensions of real engineered parts. Material addition is modeled via meta-layers comprising the dimension of many physical powder layers (cf. Zaeh *et al.*[68]), though in our case the energy is deposited in a coarse, serpentine pattern, rather than instantaneously over an entire layer. Early efforts have been encouraging. Fig. 16 shows a comparison of experimental and simulation results, in particular, contours of normal stress magnitude on the mid-plane of a 316L specimen 3 cm tall. The experimental characterization, made with the build plate still attached, fused in-volume neutron diffraction measurements with digital image correlation

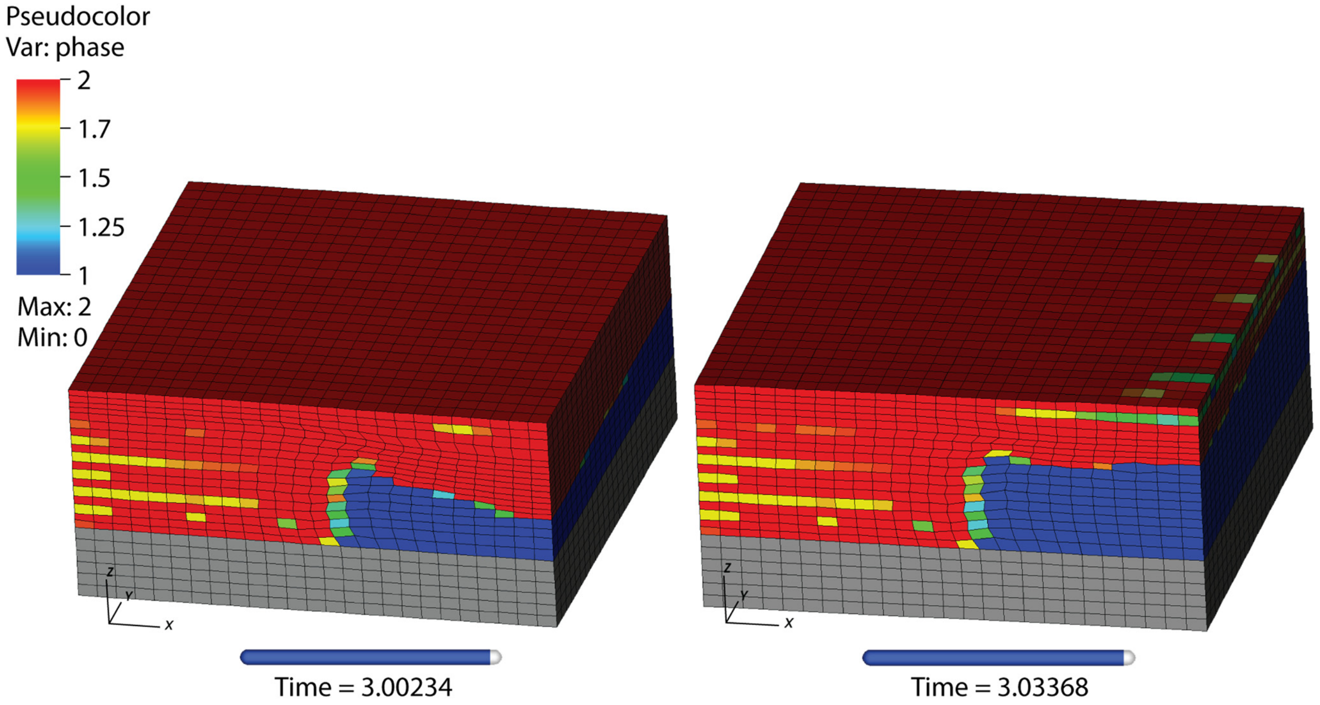

FIG. 15. A comparison of results from two overhang fabrication scenarios. The domains are 1-mm-square in plan form. The grey base represents the build plate, blue untransformed powder, and red fully transformed material. The first scenario maintains constant laser power throughout the build scans. The second scenario modulates the laser power whenever the scans extend into the overhang section, leading to a more uniform build thickness.

(DIC) on the side-surfaces.[76] The simulation results are plotted with identical color ranges and display the ability of the finite element analysis to capture the high compressive stresses in the interior of each arm, balanced by surrounded tensile stress. Further refinements are being pursued, both for physics representation and computational efficiency.

F. Alternative approaches

The majority of academic researchers use commercial Computer-Aided Engineering (CAE) software modeling tools. This reflects both a lack of native software assets within these research teams as well as a pragmatic recognition that commercial tools are the most likely avenues for subsequent industrial adoption. This choice allows these researchers to leverage software with a rich feature set, yet also places some key restrictions on their modeling approaches. First, having no ability to customize/extend the software, they must rely upon the publically documented interfaces allowing specification of simulation components such as user-defined boundary conditions and material models. Furthermore, these software tools typically can still only leverage modest computational resources, thus limiting the size of the computational mesh utilized. Within this context, insightful efforts have been achieved by teams such as Zaeh and co-workers.[68] There, a simple part geometry is accreted through a succession of meta-layers, each 1 mm thick, hence representing a collection of roughly 20 actual powder layers. Simultaneous cooling of an entire meta-layer from an assigned temperature of T_{solidus} captures the overall bending behavior induced in the test fabrication, but clearly cannot capture more local behaviors influenced by specifics of the laser scanning strategy. More recently, that team has developed a means of abstracting the true laser scan paths to identify areal boxes in the plane of the active meta-layer.[77] This abstraction considers the laser scan strategy on a subset of the true powder layers comprising the

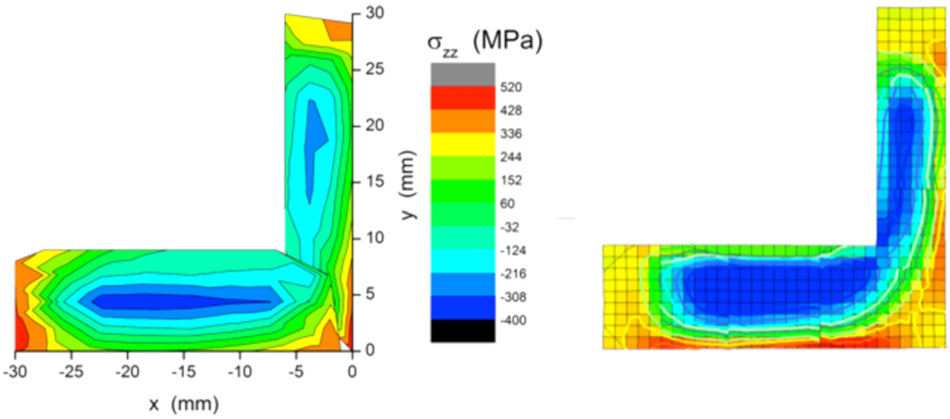

FIG. 16. A comparison of normal stress at the mid-plane of a 316L specimen assessed experimentally (left) combining neutron diffraction and digital image correlation[76] to a thermo-mechanical finite element simulation.

meta-layer, arriving at an aggregate heat load applied to successive planar areas. Results for improved fidelity are promising.[75] It is interesting to note that this team often utilizes a "one-way" coupled approach, where a thermal solution for the part formation is pre-computed and then utilized by a subsequent mechanics-only simulation of the stress response.

Academic modeling research has not been solely focused upon commercial software. One example of this is the work by Stucker and his research team. Pal *et al.*[78] summarize a series of numerical algorithms they have explored with the goal of significantly reducing the computational cost for finite element simulation of the SLM process. For instance, a limited volume of fine mesh near the active melt region incrementally traverses a coarse mesh representation of the entire part volume. They have also explored reusing significant parts of the stiffness matrix to reduce costs associated with numerical linear algebra. The size of the thermal problem is further reduced by representing the coarse-mesh, far-field temperature field through a basis constructed from a small number of eigenvectors. Publications to date have not documented the complete integration of all these numerical technologies, and that process is now being pursued in the context of a commercial start-up. We also note that this team has demonstrated to date perhaps the most complex material constitutive model for SLM applications, a crystal plasticity representation incorporating dislocation density.[79]

V. ROLE OF DATA MINING AND UNCERTAINTY QUANTIFICATION (UQ)

The use of modeling and simulation to gain insight into the physical processes that govern additive manufacturing (AM) is one step in the process of part qualification. To fully understand the factors that influence part quality and to provide a confidence interval on the properties of a part produced using AM, we also need experiments, data mining, and statistical inference. The role of the experiments is in validating the simulations to ensure that the computer model adequately represents reality.[80] Data mining techniques allow us to extract useful information from both simulations and experiments, providing insight and efficiencies in building parts with desired properties. Statistical inference enables us to reason in the presence of uncertainties; these could be uncertainties in either the experiments or the simulations.

This section provides a glimpse into some of the many ways in which ideas from the multi-disciplinary, and often overlapping, fields of data mining, statistics, and uncertainty analysis can be used in AM. Since the application of these ideas in AM is relatively new, this overview is necessarily introductory in nature. It is not intended to be a comprehensive review or comparison of techniques. Instead, we address two questions associated with AM: first, how do we select the different process parameters to build a part, and second, how do we quantify the uncertainties in the properties of a part?

A. Building AM parts with desired properties

Determining the optimal parameters required to create a part with a desired property, such as density >99%, is often challenging, requiring extensive experimentation. This is because the number of parameters that control the AM process is large, numbering over a hundred by some estimates.[13] This optimization process unfortunately has to be repeated with changes in the material or the property being optimized, as well as changes in the machine parameters, such as the laser power or beam spot size. Modeling and simulation can play an important role in reducing the costs of this process optimization. We next describe briefly several of the current approaches that rely mainly on experimentation and compare them with an approach we have recently proposed that combines experiments with simulations using data mining techniques. We focus on part density, as this is one of the first properties needing to be optimized in building an additively manufactured part. We describe the approach using 316L stainless steel as an example, though the ideas can be applied to other materials and other properties as well.

1. Design of computational and physical experiments

There have been several studies that primarily use experiments to determine the process parameters that result in high-density parts. The approach taken is based on one or more of the following: (i) selecting parameters based on theory where the energy density, defined as a function of laser speed, power, and scan spacing, is restricted to lie within certain predetermined values; (ii) implementing simple single-track experiments to identify parameters that result in a sufficiently deep melt pool; (iii) building small pillars using various combinations of parameters and determining their density; and (iv) combining experiments with ideas from the field of design of experiments.

Single-track experiments[52] are a simple way to determine which combinations of laser power and speed result in melt pools that are deep enough to melt through the powder layer into the substrate. A layer of powder of a specified thickness is spread on a thin plate and several tracks, at varying laser power and speeds, are created. The plate is then cut, the cross-section is etched and polished to reveal the melt-pool perpendicular to the laser track, and the melt-pool characteristics are obtained, as shown in Fig. 17. Both the top view of the tracks and the melt-pool characteristics provide useful insight into the surface roughness, the continuity of the track, and the depth and width of the melt pool. With increasing power or reduced speed, the melt pool becomes deeper, as shown in the three examples on the right of Fig. 17. For high-density parts, we need to select parameters that locally reduce porosity by ensuring (i) that the powder melts completely, removing any voids in the powder bed, and (ii) that the process does not enter key-hole mode melting, where the laser can drill deep into the substrate, resulting in vaporization and formation of voids.[31] A simple way to improve the efficiency of the single-track experiments is to use a tilted plate[81] so that several powder layer thicknesses can be evaluated using a single track.

While a suitable choice of the laser power and speed can ensure sufficient melting locally for a given powder layer thickness, the density of a part is also determined by other processing parameters, including the overlap between

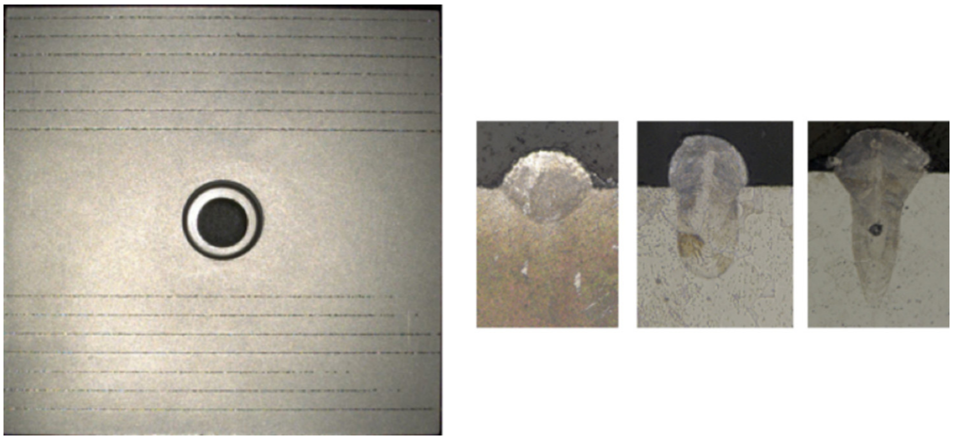

FIG. 17. On the left, a small build plate, 40 mm × 40 mm in dimensions, with 14 single tracks. The plate is tilted, so that when a layer of powder is spread, its thickness is zero at the left edge, and increases linearly to 200 μm at the right edge. Once each track has been created using a specified laser power and speed, the plate can be cut at various powder thickness values to obtain the cross-section of the track, as shown on the right for three sample tracks.

adjacent scan lines and the scanning strategy that determines how the area in one layer is scanned and how the scan pattern in one layer is related to the scan pattern in the next layer. A fully experimental approach to study the effect of these parameters was used by Yasa *et al.*[6,82] who built small pillars using different parameter settings and evaluated their density using the Archimedes method. A slightly different approach was used by Kempen *et al.*[83] who started with single-track experiments and used the quality of the tracks to identify a process window for building pillars for density evaluation.

As the design space of AM machines has expanded with the use of higher-powered lasers, new scanning strategies, new materials, and new processing techniques, ideas from the field of design of experiments[84,85] have started to play a role in systematic studies to understand the influence of various parameters on properties of parts. This field is relevant to understanding the design space of both experiments as well as simulations, which are sometimes referred to as computational experiments. It provides guidance on the selection of parameters and their values, as well as the analysis of the results. For example, Delgado *et al.*[86] used a full factorial experimental design with three factors (layer thickness, scan speed, and build direction) and two levels per factor in their study on part quality for a fixed laser power. The outputs of interest were dimensional accuracy, mechanical properties, and surface roughness. The results of the experiments were analyzed using an ANOVA (Analysis Of VAriance) approach to understand the effects of various factors on the outputs.

We have recently developed an approach to process optimization for high-density parts that exploits both simulations and experiments by combining the insight from each using data mining and statistical techniques.[87] Since multiscale simulations, as well as experiments involving single tracks and pillars, can be very expensive, we developed an iterative approach that starts with simple simulations and experiments and uses the results to guide the choice of parameters for more complex simulations and experiments.

We first used a very simple, and computationally inexpensive, Eagar-Tsai model[88] to explore the design space. This model considers a Gaussian beam on a flat plate to describe conduction-mode laser melting. The temperature distribution is then used to compute the melt-pool width, depth, and length as a function of four input parameters—laser power, laser speed, beam size, and laser absorptivity of the powder. The Eagar-Tsai model does not directly relate the process parameters to the density of a part. Further, it does not consider powder other than the effect of powder on absorptivity, so its results provide only an estimate of the melt-pool characteristics. However, it is a simple model, making it computationally inexpensive. This means that we can sample the input parameter space rather densely to understand how the melt-pool depth and width vary with the four inputs.

2. Sampling strategies

There are many ways in which the design space of input parameters to the simulations and experiments can be sampled. Screening experiments, which are done at the initial stages of a traditional design of experiments endeavor,[89] use a large number of parameters, each sampled at two extreme points that cover the range of each parameter. For d parameters, this results in 2^d experiments. However, if the range of a parameter is large, sampling at the two extreme values might not be sufficient. If k sample values are used for each parameter, the number of experiments increases exponentially to k^d; this can become prohibitively expensive even for moderate values of k and d. Therefore, a screening experiment using just two levels is often used first to identify the important parameters, which are then sampled more frequently. Sampling of the design space is often accompanied by analysis of the results using ANOVA to determine the factors that have an effect on the response, or using response surface methods, where a first- or second-order model is fit to the data. These parametric response surfaces can also act as surrogates to the data.

The traditional approach to the design of experiments was motivated by physical experiments where it was expected that repeating an experiment would give slightly different results. More recently, similar ideas have been applied to simulations, where repetition usually does not have any effect on the results. The ideas used in the field of DACE (Design and Analysis of Computer Experiments) also involve sampling the input parameter space of the simulations and building surrogates that act as predictive models. If the sampling is adequate, the latter can be considered as providing reasonable approximations to the simulation output variables for a specific range of input parameters. These

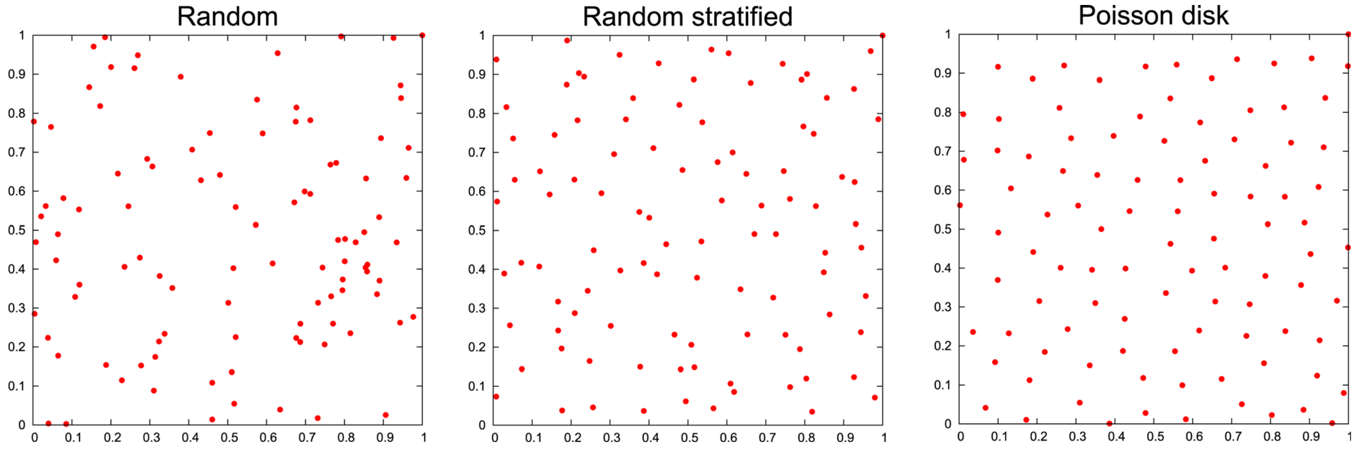

FIG. 18. 100 sample points distributed randomly in a two-dimensional space using, from left to right, random sampling, random stratified sampling, and Poisson disk sampling.

surrogates can be extremely useful in problems when the simulations are computationally very expensive.

Since the accuracy of the surrogates depends on how well the input space of parameters is sampled, but the function relating the output to the inputs is unknown, the initial set of samples is usually placed randomly and additional samples are added as necessary. Using a simple random sampling can result in regions that are under- or over-sampled, as shown in Fig. 18 for a two-dimensional domain. To address this, we used stratified sampling, where each of the four input parameters was divided into a number of levels and a point selected randomly in each of the resulting cells. As the range of values of the laser beam size and absorptivity of the powder was small, we used a smaller number of levels for these inputs in comparison with the laser power and speed parameters. Fig. 18 shows that a stratified sampling approach results in an improved placement of samples relative to a straightforward random sampling.

In our work with 316L stainless steel, we varied the speed from 50 mm/s to 2250 mm/s with 11 levels, the power from 50 W to 400 W using 7 levels, the beam size (D4σ) from 50 μm to 68 μm using 3 levels, and the laser absorptivity from 0.3 to 0.5 using 2 levels. This resulted in 462 parameter combinations that were input to our simulation. These ranges were selected as follows: The upper bound on the power was set to the peak power of our machine. The lower limit on the speed was set to ensure sufficient melting at the low power values such that the melt-pool depth would be at least 30 μm (the layer thickness selected for our experiments). The upper limit on the speed was estimated at a value that would likely result in a relatively shallow melt pool at the high power value. The lower and upper limits on the beam size were obtained from measurements of the beam size on our machine at focus offsets of 0 mm and 1 mm. By varying the beam size and the absorptivity, we were able to account for possible variations in these parameters over time or with changes in build conditions as we built the parts.

A drawback of the stratified random sampling approach is that the number of samples is determined by the number of input parameters and the number of levels in each parameter; it cannot be set to a pre-specified value. As mentioned earlier, this number can be quite large. In our work using the Eagar-Tsai model, this was not an issue as the model is computationally inexpensive. However, for more expensive models, where we want to control the number of samples by starting with a small number and incrementally adding new samples, an alternative approach using low-discrepancy sampling is often used. In a low-discrepancy sampling in two (or three) dimensions, the number of sample points falling into an arbitrary subset of the domain is proportional to the area (or volume) of the subset. This essentially results in samples that are randomly placed far apart from each other. An example of such a sampling is the Poisson disk sampling, shown in Fig. 18, where no two points are closer than a pre-specified distance.[90]

3. Feature selection

In our approach to finding optimal parameters for high part density, we were able to sample the input parameter space of the Eagar-Tsai model quite densely as it had only four input parameters. However, there are more than a hundred variables in additive manufacturing when we consider material properties, powder bed conditions, laser parameters, and so on. Some of these variables, such as material properties, are fixed for a material, though their values may not be known precisely, or may have a range associated with them. Other variables, such as the laser speed and power, are set during the manufacture of a part. Given this large number of variables, a commonly used class of algorithms in data mining, namely, dimension reduction,[91] become relevant in making the task of process optimization tractable. The dimension of a problem is the number of features or variables describing an experiment or simulation. By reducing the dimension of a problem, we can focus on just the most important variables, making it easier to understand how the outputs, such as melt pool dimensions, are related to the input variables. Further, as mentioned in Section V A 2, the number of samples required to fully cover the design space is exponential in the number of dimensions. Therefore, reducing the dimensions is important when the experiments and simulations are expensive.

There are a number of dimension-reduction algorithms, including linear and non-linear methods that transform the input parameter space into a reduced dimension space, as well as feature subset selection methods that rank the input variables, or features, in order of importance. The latter are more relevant in the context of additive manufacturing as we need to set values of specific parameters, not their linear or non-linear combinations.

One way in which these feature selection techniques can be used is for the identification of the important input parameters in the simulations. In Section V A 2, we used stratified random sampling to identify the sample points in the four-dimensional space of laser power, laser speed, beam size, and laser absorptivity. We then ran the Eagar-Tsai simulation at these sample points and obtained the melt-pool width, depth, and length. Of these melt-pool characteristics, we are most interested in the depth and the width. The depth indicates if the energy density is sufficient to melt through the powder to the substrate below. The width helps us to determine how far apart the adjacent laser tracks should be to ensure that no un-melted powder is left between the tracks.

We used two feature selection techniques to understand the order of importance of the four input variables in determining the melt-pool depth and width.

The Correlation-based Feature Selection (CFS) method[92] is a simple approach that calculates a figure of merit for a feature subset of k features defined as

$$\frac{k\,\overline{r_{cf}}}{\sqrt{k + k(k-1)\overline{r_{ff}}}},$$

where $\overline{r_{cf}}$ is the average feature-output correlation and $\overline{r_{ff}}$ is the average feature-feature correlation. We use the Pearson correlation coefficient between two vectors, X and Y, defined as

$$\frac{Cov(X,Y)}{\sigma_X \sigma_Y},$$

where $Cov(X,Y)$ is the covariance between the two vectors, and σ_X is the standard deviation of X. A higher value of merit results when the subset of features is such that they have a high correlation with the output and a low correlation among themselves.

The mean-squared error (MSE) method: In the second feature selection method, the features are ranked using the MSE as a measure of the quality of a feature.[93] This metric is used in regression trees (Section V A 4) to determine which feature to use to split the samples at a node of the tree. Given a numeric feature x, the feature values are first sorted $x_1 < x_2 < \ldots < x_n$. Then, each intermediate value, $(x_1 + x_{1+1})/2$, is proposed as a splitting point, and the samples are split into two depending on whether the feature value of a sample is less than the splitting point or not. The MSE for a split A is defined as

$$MSE(A) = p_L\, s(t_L) + p_R\, s(t_R),$$

where t_L and t_R are the subset of samples that go to the left and right, respectively, by the split based on A, p_L and p_R are the proportion of samples that go to the left and right, and *s(t)* is the standard deviation of the *N(t)* output values, c_i, of samples in the subset t, defined as

$$s(t) = \sqrt{\frac{1}{N(t)} \sum_{i=1}^{N(t)} \left(c_i - \overline{c(t)}\right)^2},$$

where $\overline{c(t)}$ is the mean of the values in the subset t. For each feature, the minimum MSE across the values of the feature is obtained, and the features are rank ordered by increasing values of their minimum. This method considers a feature to be important if it can split the data set into two, such that the standard deviation of the samples on either side of the split is minimized, that is, the output values are relatively similar on each side. Note that unlike CFS, which considers subsets of features, this method considers each feature individually.

Table III presents the ordering of subsets of input features by importance for the melt-pool width, length, and depth obtained using the CFS method. A noise feature was added as another input; this is consistently ranked as the least important variable, as might be expected. The table indicates that for the melt-pool depth and width, the single most important input is the speed, while the top-two most important inputs are the speed and power. In contrast, for the length of the melt pool, the top-two two most important inputs are power and absorptivity.

Table IV presents the results for the MSE method. These are very similar to the CFS method, with the exception that the beam size is ranked lower than the noise variable for the depth of the melt pool. For all three melt-pool characteristics, the three lowest ranked variables have the MSE value roughly the same, so the corresponding three variables have roughly the same order of importance.

These results indicate that we should focus on the laser power and speed as they are the most important inputs related to the melt-pool depth and width based on the Eagar-Tsai simulations. While these simple simulations relate just four inputs to the melt-pool characteristics, we expect that as we move to more complex simulations, feature selection and other dimension reduction techniques will become more useful in helping us to focus on the important variables, potentially limiting the number of experiments or simulations required to create parts with desired properties.

TABLE III. Order of importance of subsets of features using the CFS method. A higher rank indicates a more important input; the best subset of features is the one with the highest ranks.

	Speed	Power	Beam size	Absorptivity	Noise
Width	5	4	2	3	1
Length	3	5	2	4	1
Depth	5	4	2	3	1

TABLE IV. Order of importance of subsets of features using the MSE method. A higher rank indicates a more important input.

	Speed	Power	Beam size	Absorptivity	Noise
Width	5	4	2	3	1
Length	3	5	2	4	1
Depth	5	4	1	3	2

4. Data-driven predictive modeling

Our simulations using the Eagar-Tsai model provide the melt-pool characteristics at specific input values. These simulation inputs and outputs can also be used to build a data-driven predictive model, or a surrogate, that can be used to predict the output values at other inputs. A simple predictive model is a regression tree,[93] which is similar to a decision tree, but with a continuous instead of a discrete output.

A regression tree is a structure that is either a leaf, indicating a continuous value, or a decision node that specifies some test to be carried out on a feature, with a branch and sub-tree for each possible outcome of the test. If the feature is continuous, there are two branches, depending on whether the condition being tested is satisfied or not. The decision at each node of the tree is made to reveal the structure in the data. Regression trees tend to be relatively simple to implement, yield results that can be interpreted, and have built-in dimension reduction.

Regression algorithms typically have two phases. In the training phase, the algorithm is “trained” by presenting it with a set of examples with known output values. In the test phase, the model created in the training phase is tested to determine how accurately it performs in predicting the output for known examples that were not used in training. If the results meet expected accuracy, the model can be put into operation to predict the output for a sample point, given its inputs.

The test at each node of a regression tree is determined by examining each feature and finding the split that optimizes an impurity measure. We use the mean-squared error, MSE, as defined in Section V A 3, as the impurity measure. The split at each node of the tree is chosen as the one that minimizes MSE across all features for the samples at that node. To avoid splitting the tree too finely, we stop the splitting if the number of samples at a node is less than 5 or the standard deviation of the values of the output variable at a node has dropped below 5% of the standard deviation of the output variable of the original data set.

There are different ways in which we can evaluate the accuracy of the regression trees. The first is k runs of m-fold cross validation, where the data are divided randomly into m equal parts, the model is trained on (m-1) parts, and evaluated on the part that is held out. This is repeated for each of the m parts. The process is repeated k times, each with a different random partition of the data. The final accuracy metric is the average of the accuracy for each of the k m parts. We use the relative mean-squared error metric, defined as

$$\sum_{i=1}^{n}(p_i - a_i)^2 \Big/ \sum_{i=1}^{n}(\bar{a} - a_i)^2,$$

where p_i and a_i are the predicted and actual values, respectively, of the i-th sample point in the test data consisting of n points, and $\bar{a}$ is the average of the actual values in the test data. This is essentially the ratio of the variance of the residual to the variance of the target (that is, actual) values and is equal to $(1.0 - R^2)$, where R^2 is the coefficient of determination. The second metric is the prediction using a leave-one-out (LOO) approach, where a model, which is built using all but one of the sample points, is used to predict the value at the point that is held out. For a data set with N points, this is essentially N-fold cross validation.

A common approach to improving the accuracy of regression algorithms is to use an ensemble, where many models, built from the same training data using randomization, are created.[91] The final prediction is the mean of the prediction from each of the models. In our work, we consider 10 trees in the ensemble, with randomization introduced through sampling. Instead of using all the sample points at a node of the tree to make a split, we use a random subset of the samples, thus making each tree in the ensemble different from the others.

Fig. 19 shows the accuracy of the regression tree model in predicting the depth using the 462 simulations of the Eagar-Tsai model as the training set. Panels (a) and (b) show the predicted vs. actual values using LOO for 1 tree and 10 trees, respectively. We observe that most of the points are near the blue line at 45 degrees (indicating perfect prediction), though the scatter is greater at larger melt-pool depths. The scatter reduces with the use of ensembles as would be expected. Using 5 runs of 5-fold cross validation as the error metric, we obtain a relative mean-squared error of 8% with a single tree and 3.6% with an ensemble of 10 trees.

The regression tree acts as a surrogate for the data from the Eagar-Tsai simulations and can be used to predict the width, depth, and length of the melt pool for a given set of inputs. The inputs for a sample point are used to traverse the tree, following the decision at each node, until a leaf node is

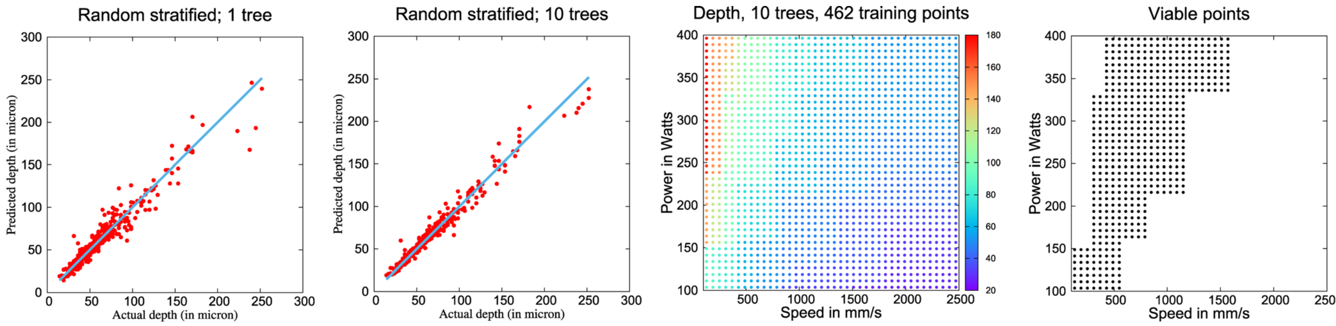

FIG. 19. From left to right: The predicted versus actual depth using LOO for 1 tree and 10 trees, respectively; the predicted depth on a 40 × 40 grid in the power-speed space and the resulting viable sample points.

reached; the predicted value assigned to the sample is the mean of the output values of the training data that end up at that leaf node. Fig. 19(c) shows the depth prediction at sample points on a 40 × 40 grid over the power-speed design space, using a fixed value of $D4\sigma = 52\,\mu$m and absorptivity of 0.4 for 316L stainless steel. The prediction was obtained using the 462 Eagar-Tsai points to build a model with 10 regression trees. Panel (d) shows the viable space in the power-speed plot, where viability is defined as any grid point with predicted depth greater than, or equal to, 60 μm and less than, or equal to, 120 μm. In comparison with the Eagar-Tsai simulations, where each simulation takes approximately 1 min on a laptop, it takes a few microseconds to build the regression tree surrogate from the 462 simulations and practically no time to generate the melt-pool depth for a set of input variables using the surrogate.

5. Example of density optimization

The Eagar-Tsai model, combined with sampling techniques, feature selection, and the building of data-driven predictive models, enables us to determine the melt-pool characteristics for a given power and speed combination. The accuracy of these predictions depends on the number and location of the sample points, the accuracy of the physics model, as well as the complexity of the function being predicted. The Eagar-Tsai model, being relatively simple, gives us an approximation of the melt-pool characteristics. We use it to determine the viable region of the power-speed space (these being the most important variables) and then select a few points in this region for single-track experiments, as shown in Fig. 17. Once we know the actual melt-pool characteristics at specific power-speed values, we can use them to identify process parameters for building small, three-dimensional pillars, whose density is measured using the Archimedes method.

Fig. 20 shows the first set of 24 pillars of 316L stainless steel in powder, along with the density for the first two sets of pillars. Each pillar is 10 mm × 10 mm × 8 mm. The rows correspond to different power values, while the columns represent different speeds. Having obtained the density estimate for the first set of 24 pillars, we ran another 24 at the same power values, but with the speeds chosen to complete the gaps in the density curves.[87]

We have successfully used this approach to build high-density parts for several different materials and powders of different sizes. While our early work used a tilted plate for single-track experiments, we found that we typically used only one value for powder layer thickness. As a result, it was more efficient to use a flat plate. This also allowed us to double the number of tracks on a plate, leading to better exploration of the power-speed space using experiments.

B. Uncertainty analysis

There are many ways in which we can use simulations and experiments, both simple and complex ones, in additive manufacturing. In Subsection V A, we outlined a process by which we can combine simple simulations with experiments to create an approach that efficiently identifies the process parameters for high-density parts. However, we expect that the conditions under which a part is built will vary even if we set the parameters to certain fixed values. For example, the laser beam size may change as the optics get heated during use, or the porosity of the powder bed may vary depending on the distribution of powder particles in a layer, or the powder size distribution may vary with re-use, or the calibration of the laser power, speed, and beam size may change over time. All these variations will influence the properties of the part being built.

As we start using additively manufactured parts in situations where their failure could have serious consequences, it becomes important to quantify how much variation we can expect in the part resulting from variations in the inputs. This quantification of the uncertainty in the properties of a part, such as its density or dimensions, is an important step in qualification and certification of AM parts. Such issues are not restricted to experiments alone. In the case of simulations, it is not just the input parameters, such as laser power and beam size, that might vary. Other variables in the simulations, such as the material properties, may not be known precisely, or may be known within a certain range. We then need to understand the sensitivity of the simulation outputs to these variations in the inputs and material properties.

One approach to addressing these questions is to build many parts over time with the same set of parameters, and evaluate their properties, or run many simulations, varying the parameters over their expected range, and evaluate the range of output values. This can be prohibitively expensive,

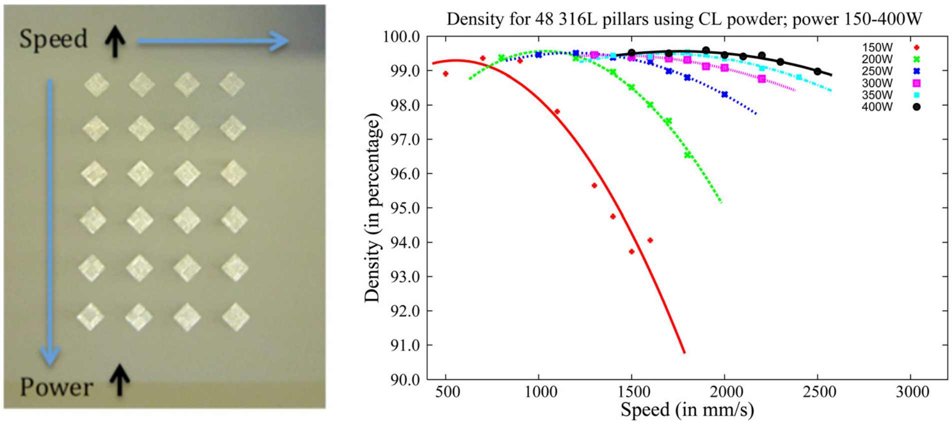

FIG. 20. On the left, 24 pillars from the first set in powder; speed increases from left to right and power increases from top to bottom. On the right, the density of pillars from the first two sets, built using 316L powder from Concept Laser (CL) on a CL M2 machine.

especially when the simulations are computationally intensive and measuring the properties of the parts is time consuming and labor intensive. An alternative is to use uncertainty analysis techniques from statistics and machine learning.[80] The application of these ideas in AM is at the very early stages, though they are being applied in other domains. We next present some preliminary thoughts on the ways in which we can address uncertainty issues in AM.

In Section V A 4, we used a regression tree surrogate model for predicting the depth of the melt pool, with the model built from Eagar-Tsai simulations run at various sample points in the design space. Another class of predictive models, referred to as Gaussian process models[94] provide not only a prediction, but also an associated uncertainty. These techniques can be applied to simulation data, where the simulations run at specific points are used to constrain the uncertainty in the predictions, as well as experimental data, where the experiments, run at specific sample points, also have associated uncertainties that are used to evaluate the uncertainty at new sample points.

The idea of ensembles described in Section V A 4 can also be used to obtain an idea of the uncertainty due to the surrogate model. Since each regression tree in the ensemble will provide a slightly different result, the spread of values will reflect how much we can expect the results to vary as we build regression models with slightly different training data.

VI. FUTURE APPLICATIONS

A. Powder model

The powder model is a powerful tool to study and optimize various aspects of the additive manufacturing process. These include:

- Understanding the effects of laser power, speed, beam size, shape, and profile[95–97]
- Understanding the effects of powder size distribution and packing density
- Developing parameters for new materials
- Guiding development of alloys specifically engineered for additive manufacturing
- Understanding the effects that control surface finish
- Understanding the effects that control “sparks” and “spatter.” (Spatter is molten metal droplets that are ejected from the melt pool.)

Using the powder model is much more economical in terms of time and cost compared with carrying out experiments in an additive manufacturing system, particularly a commercial system where such studies may be prohibited by the manufacturer. With this capability, it is possible to help define the additive manufacturing systems of the future.

B. Effective medium model

Proper effective medium models can be utilized to computationally explore a number of issues regarding part design and fabrication SLM processes:

- Predict the deformations occurring during fabrication and thus evaluate the possibility of process breakdown or out-of-tolerance end product
- Predict the residual stresses from fabrication and thus provide initial conditions for evaluating their impact on a design’s intended performance
- Develop parameters that can be used to improve the quality of challenging configurations through examination of representative geometries such as:
  - Unsupported downward-facing surfaces
  - Thin walls
  - Horizontal holes
  - Vertical holes
  - Unsupported overhangs
  - Unsupported bridges
- Provide histories of local, configuration-specific temperatures, and temperature gradients to help assess the likely resulting material microstructures
  - Permit full initial condition to assess the effects of post-processes such as heat treatment
  - Provide the basis for reduced order models that can be integrated with control systems on SLM machines.

Part scale modeling would also be the likely point-of-intersection with part design optimization, and one can envision combining design and process identification under a multi-objective optimization framework.

C. Solving the inverse problem

Both the powder and effective medium models will be essential elements underpinning the solution of the inverse problem (solving the inverse problem involves “use of the actual results of some measurements of the observable parameters to infer the actual values of the model parameters.”[98]). That is, specifying desired properties and using optimization to find the voxel-by-voxel parameters for building a part. Because of the long computational times required to compute a full part at high resolution using the physics-based models described here, an alternate approach is required to control the process better and identify the stable operating regimes for qualification. This involves approximating the large-scale simulations with low-computational-cost surrogates. Since powder bed fusion is a complex process, it is necessary to identify the important “science” in the regimes of interest. By focusing on the important science and ignoring the less important, we can identify optimized build direction, optimized support structures, and implement an intelligent feed forward capability.

VII. SUMMARY AND CONCLUSIONS

A. Powder model

The powder model combines in three dimensions the laser beam interaction with the powder with the thermo-mechanical response of the powder bed material through melt and eventual resolidification. The method incorporates as inputs many of the process parameters that may be varied for optimization of SLM for a particular material. The inclusion of many of the important physical processes in the metal's response to the laser beam allows valuable insights to be obtained into the physics of the SLM process. Outputs from the powder model can be used for inputs to other models, for example, temperature histories for microstructural modeling, or the outputs may be directly useable, such as surface roughness estimates. The powder model is an important part of the suite of tools needed to optimize SLM builds and eventually certify the fabricated parts for use.

B. Effective medium model

Effective medium models provide an abstraction to examine larger-scale phenomenon in a computationally tractable manner that can support the engineering design process in a timely manner. One should anticipate a continuing evolution of approaches, with alternatives building upon general commercial software, adapting in-house tools, and developing dedicated solutions. As analysis of real-world part configurations is the overall objective, and an important consideration will be forging the software links supporting transfers between the geometry specification, the machine scan specification, and the actual simulation. This breadth across the part scale will be complemented by more formal interchanges of information with the powder-scale model and eventual microstructure models, as well as integration with formal process and design optimization.

C. Data mining and UQ

Data mining techniques are being used to extract useful information from simulations and experiments, providing insight and efficiencies in building parts with desired properties. These techniques have been used to identify process parameters for high-density parts for a variety of materials. They can be combined with uncertainty analysis to understand how uncertainties in process parameters will affect the properties of a part, or uncertainties in input parameters and material properties used in a simulation will influence the output. When combined with experiments, techniques from data mining and uncertainty analysis will form an integral part of qualification and certification of the additive manufacturing process.

ACKNOWLEDGMENTS

This work was performed under the auspices of the U.S. Department of Energy by Lawrence Livermore National Laboratory under Contract No. DE-AC52-07NA27344. This work was funded by the Laboratory Directed Research and Development Program at LLNL under project tracking code 13-SI-002.

[1] ASTM International, *Standard Terminology for Additive Manufacturing Technologies* (ASTM International, West Conshohocken, PA, 2010).

[2] T. T. Wohlers, *Wohlers Report 2014 Additive Manufacturing and 3D Printing State of the Industry Annual Worldwide Progress Report* (Wohlers Associates, Inc, Fort Collins, Colorado, 2014).

[3] S. Srivatsa, *Additive Manufacturing (AM) Design and Simulation Tools Study* (Air Force Research Laboratory, Wright-Patterson Air Force Base, OH, 45433, 2014).

[4] Knowledge Based Process Planning and Design for Additive Layer Manufacturing (KARMA), Detailed report on Laser Cusing, SLA, SLS and Electron Beam Melting (including technical, economical and safety features) (Valencia (ESPAÑA), Report No. DL 1.1, 2011.

[5] T. Craeghs, Ph.D. thesis, University of Leuven, 2012.

[6] E. Yasa, Ph.D. thesis, Katholieke Universiteit Leuven, 2011.

[7] L. Adams, *MICROmanufacturing* (Don Nelson, Northfield, IL, 2013), Vol. SEPTEMBER/OCTOBER, p. 44.

[8] PWC, *3D Printing and the New Shape of Industrial Manufacturing* (PricewaterhouseCoopers LLP, Delaware, 2014).

[9] J. Coykendall, M. Cotteleer, J. Holdowsky, and M. Mahto, *3D Opportunity in Aerospace and Defense* (Deloitte University Press, Washington, DC, 2014).

[10] D. L. Bourell, M. C. Leu, and D. W. Rosen, *Roadmap for Additive Manufacturing Identifying the Future of Freeform Processing* (The University of Texas at Austin, Austin TX, 2009).

[11] Energetics Incorporated, *Measurement Science Roadmap for Metal-Based Additive Manufacturing* (Energetics Incorporated, Columbia, Maryland, 2013).

[12] R. Berger, *Additive Manufacturing: A Game Changer for the Manufacturing Industry?* (Roland Berger Strategy Consultants GmbH, Munich, 2013).

[13] I. Yadroitsev, *Selective Laser Melting: Direct Manufacturing of 3D-Objects by Selective Laser Melting of Metal Powders* (LAP Lambert Academic Publishing, Saarbrücken, 2009).

[14] J. P. Kruth, P. Mercelis, J. Van Vaerenbergh, and T. Craeghs, *Feedback Control of Selective Laser Melting* (Taylor & Francis Ltd, London, 2008), p. 521.

[15] T. Craeghs, F. Bechmann, S. Berumen, and J. P. Kruth, in *Proceedings of the Laser Assisted Net Shape Engineering 6 (LANE 2010), Part 2*, edited by M. Schmidt, F. Vollertsen, and M. Geiger (Elsevier Science Bv, Amsterdam, 2010), Vol. 5, p. 505.

[16] T. Craeghs, S. Clijsters, J.-P. Kruth, F. Bechmann, and M.-C. Ebert, Phys. Proc. **39**, 753 (2012).

[17] S. Clijsters, T. Craeghs, and J. P. Kruth, *A priori Process Parameter Adjustment for SLM Process Optimization* (CRC Press-Taylor & Francis Group, Boca Raton, 2012), p. 553.

[18] W. Frazier, J. Mater. Eng. Perform. **23**(6), 1917 (2014).

[19] See http://www.realizer.com/rdesigner for information on a feed forward capability.

[20] J. D. Williams and C. R. Deckard, Rapid Prototyping J. **4**(2), 90 (1998).

[21] S. Kolossov, E. Boillat, R. Glardon, P. Fischer, and M. Locher, Int. J. Mach. Tools Manuf. **44**(2–3), 117 (2004).

[22] K. Dai, X. X. Li, and L. L. Shaw, Rapid Prototyping J. **10**(1), 24 (2004).

[23] I. A. Roberts, C. J. Wang, R. Esterlein, M. Stanford, and D. J. Mynors, Int. J. Mach. Tools Manuf. **49**(12–13), 916 (2009).

[24] N. Contuzzi, S. Campanelli, and A. D. Ludovico, Int. J. Simul. Model. **10**(3), 113 (2011).

[25] M. Matsumoto, M. Shiomi, K. Osakada, and F. Abe, Int. J. Mach. Tools Manuf. **42**(1), 61 (2002).

[26] A. Hussein, L. Hao, C. Yan, and R. Everson, Mater. Des. **52**(0), 638 (2013).

[27] M. Zaeh and G. Branner, Prod. Eng. **4**(1), 35 (2010).

[28] P. Fischer, V. Romano, H. P. Weber, N. P. Karapatis, E. Boillat, and R. Glardon, Acta Mater. **51**(6), 1651 (2003).

[29] N. K. Tolochko, M. K. Arshinov, A. V. Gusarov, V. I. Titov, T. Laoui, and L. Froyen, Rapid Prototyping J. **9**(5), 314 (2003).

[30] A. V. Gusarov and I. Smurov, Phys. Proc. **5**, 381 (2010).

[31] W. E. King, H. D. Barth, V. M. Castillo, G. F. Gallegos, J. W. Gibbs, D. E. Hahn, C. Kamath, and A. M. Rubenchik, J. Mater. Process. Technol. **214**(12), 2915 (2014).

[32] N. K. Tolochko, T. Laoui, Y. V. Khlopkov, S. E. Mozzharov, V. I. Titov, and M. B. Ignatiev, Rapid Prototyping J. **6**(3), 155 (2000).

[33] A. V. Gusarov and J. P. Kruth, Int. J. Heat Mass Transfer **48**(16), 3423 (2005).

[34] X. C. Wang, T. Laoui, J. Bonse, J. P. Kruth, B. Lauwers, and L. Froyen, Int. J. Adv. Manuf. Technol. **19**(5), 351 (2002).

[35] C. Boley, S. Khairallah, and A. Rubenchik, Appl. Opt. **54**(9), 2477 (2015).

[36] FRED is distributed by Photon Engineering, LLC, Tucson, AZ.

[37] E. D. Palik, *Handbook of Optical Constants of Solids* (Academic Press, Orlando, 1985).

[38] G. Friedman, *ParticlePack User's Manual* (Lawrence Livermore National Laboratory, Livermore, CA, 2011).

[39] P. Meakin and R. Jullien, J. Phys. **48**(10), 1651 (1987).

[40] E. J. R. Parteli, in *Powders and Grains 2013*, edited by A. Yu, K. Dong, R. Yang *et al.* (American Institute of Physics, Melville, 2013), Vol. 1542, p. 185.

[41] I. Kovaleva, O. Kovalev, and I. Smurov, Phys. Proc. **56**(0), 400 (2014).

[42] E. J. R. Parteli and T. Pöschel, Powder Technol. **288**, 96 (2016).

[43] R. M. Kelkar, T. Anderson, P. Wang, and D. Bartosik, *DMLM: Effect of Bi-Modal Particle Size Distribution on Surface Finish* (Additive Manufacturing with Powder Metallurgy, 2014).

[44] A. B. Hopkins, F. H. Stillinger, and S. Torquato, Phys. Rev. E **88**(2), 022205 (2013).

[45] A. M. Prokhorov, V. I. Konov, I. Ursu, and N. Mihailescu, *Laser Heating of Metals* (A. Hilger, Bristol, Philadelphia, 1990).

[46] A. M. Rubenchik, S. S. Q. Wu, V. K. Kanz, M. M. LeBlanc, W. H. Lowdermilk, M. D. Rotter, and J. R. Stanley, Opt. Eng. **53**(12), 122506 (2014).

[47] R. W. McVey, R. M. Melnychuk, J. A. Todd, and R. P. Martukanitz, J. Laser Appl. **19**(4), 214 (2007).

[48] R. P. Martukanitz, R. M. Melnychuk, M. S. Stefanski, and S. M. Copley, J. Laser Appl. **19**(4), 214 (2007).

[49] A. Rubenchik, S. Wu, S. Mitchell, I. Golosker, M. LeBlanc, and N. Peterson, Appl. Opt. **54**(24), 7230 (2015).

[50] V. Y. Bodryakov, High Temp. **51**(2), 206 (2013).

[51] See http://app.knovel.com/hotlink/toc/id:kpRVTPSCA1/recommended-values-of for recommended values of thermophysical properties for selected commercial alloys.

[52] I. Yadroitsev, A. Gusarov, I. Yadroitsava, and I. Smurov, J. Mater. Process. Technol. **210**(12), 1624 (2010).

[53] A. V. Gusarov and E. P. Kovalev, Phys. Rev. B **80**(2), 024202 (2009).

[54] M. Rombouts, L. Froyen, A. V. Gusarov, E. H. Bentefour, and C. Glorieux, J. Appl. Phys. **97**(2), 013533 (2005).

[55] S. I. Anisimov, High Temp. **6**(1), 110 (1968).

[56] S. I. Anisimov, Sov. Phys. JETP-USSR **27**(1), 182 (1968).

[57] C. J. Knight, AIAA J. **17**(5), 519 (1979).

[58] A. Klassen, T. Scharowsky, and C. Korner, J. Phys. D: Appl. Phys. **47**(27), 275303 (2014).

[59] S. I. Anisimov and V. A. Khokhlov, *Instabilities in Laser-Matter Interaction* (CRC Press, Boca Raton, Florida, 1995).

[60] R. Rai, J. W. Elmer, T. A. Palmer, and T. DebRoy, J. Phys. D: Appl. Phys. **40**(18), 5753 (2007).

[61] G. G. Gladush and I. Smurov, *Physics of Laser Materials Processing: Theory and Experiment* (Springer, Berlin, 2011).

[62] D. Steinberg, Lawrence Livermore National Laboratory, Report No.UCRL-MA-106439, 1996.

[63] C. Körner, E. Attar, and P. Heinl, J. Mater. Process. Technol. **211**(6), 978 (2011).

[64] C. Körner, A. Bauereiß, and E. Attar, Modell. Simul. Mater. Sci. Eng. **21**(8), 085011 (2013).

[65] F. J. Gurtler, M. Karg, K. H. Leitz, and M. Schmidt, in *Lasers in Manufacturing*, edited by C. Emmelmann, M. F. Zaeh, T. Graf *et al.* (Elsevier Science Bv, Amsterdam, 2013), Vol. 41, p. 874.

[66] R. Ganeriwala and T. I. Zohdi, Proc. CIRP **14**(0), 299 (2014).

[67] A. V. Gusarov, I. Yadroitsev, P. Bertrand, and I. Smurov, J. Heat Transfer **131**(7), 072101 (2009).

[68] M. F. Zaeh, G. Branner, and T. A. Krol, in *Innovative Developments in Design and Manufacturing: Advanced Research in Virtual and Rapid Prototyping*, edited by P. J. D. Bartolo, A. C. S. DeLemos, A. M. H. Pereira *et* al. (CRC Press-Taylor & Francis Group, Boca Raton, 2010), p. 415.

[69] N. E. Hodge, R. M. Ferencz, and J. M. Solberg, Comput. Mech. **54**(1), 33 (2014).

[70] J. A. Goldak and M. Akhlaghi, *Computational Welding Mechanics* (Springer, New York, 2005).

[71] L. E. Lindgren, *Computational Welding Mechanics: Thermomechanical And Microstructural Simulations* (Woodhead and Maney Pub., Cambridge, England; CRC Press, Boca Raton, 2007).

[72] P. Michaleris, Finite Elem. Anal. Des. **86**, 51 (2014).

[73] E. R. Denlinger, J. Irwin, and P. Michaleris, J. Manuf. Sci. Eng. **136**(6), 061007 (2014).

[74] J. M. Solberg, N. E. Hodge, R. M. Ferencz, I. D. Parsons, M. A. Puso, M. A. Havstad, R. A. Whitesides, and A. P. Wemhoff, Diablo User Manual Livermore, CA, Report No. LLNL-SM-651163, 2014.

[75] J. Schilp, C. Seidel, H. Krauss, and J. Weirather, Adv. Mech. Eng. **6**, 217584 (2014).

[76] A. S. Wu, D. W. Brown, M. Kumar, G. F. Gallegos, and W. E. King, Metall. Mater. Trans. A **45**(13), 6260–6270 (2014).

[77] C. Seidel, M. F. Zaeh, M. Wunderer, J. Weirather, T. A. Krol, and M. Ott, Proc. CIRP **25**(0), 146 (2014).

[78] D. Pal, N. Patil, K. Zeng, and B. Stucker, J. Manuf. Sci. Eng.-Trans. ASME **136**(6), 061022 (2014).

[79] D. Pal, N. Patil, and B. E. Stucker, paper presented at the International Solid Freeform Fabrication Symposium–An Additive Manufacturing Conference Austin, Texas (2012).

[80] National Research Council, *Assessing the Reliability of Complex Models: Mathematical and Statistical Foundations of Verification, Validation, and Uncertainty Quantification* (The National Academies Press, Washington, DC, 2012).

[81] I. Yadroitsev and I. Smurov, Phys. Proc. Part B **5**(0), 551 (2010).

[82] J. P. Kruth, M. Badrossamay, E. Yasa, J. Deckers, L. Thijs, and J. Van Humbeeck, paper presented at the 16th International Symposium on Electromachining (ISEM XVI), Shanghai-China (2010).

[83] K. Kempen, L. Thijs, E. Yasa, M. Badrossamay, W. Verheecke, and J.-P. Kruth, in *Twenty Third Annual International Solid Freeform Fabrication Symposium—An Additive Manufacturing Conference*, edited by D. Bourell (University of Texas at Austin, Austin, Texas, USA, 2011), p. 484.

[84] G. W. Oehlert, *A first Course in Design and Analysis of Experiments* (W. H. Freeman, New York, 2000).

[85] K. Fang, R.-z. Li, and A. Sudjianto, *Design and Modeling for Computer Experiments* (Chapman & Hall/CRC, Boca Raton, FL, 2006).

[86] J. Delgado, L. Sereno, J. Ciurana, and L. Hernandez, *Methodology for Analyzing the Depth of Sintering in the Building Platform* (CRC Press-Taylor & Francis Group, Boca Raton, 2012), p. 495.

[87] C. Kamath, B. El-dasher, G. F. Gallegos, W. E. King, and A. Sisto, Int. J. Adv. Manuf. Technol. **74**(1–4), 65 (2014).

[88] T. W. Eagar and N. S. Tsai, Weld. J. **62**(12), S346 (1983).

[89] D. C. Montgomery, *Design and Analysis of Experiments* (John Wiley & Sons, Hoboken, NJ, 2004).

[90] R. Bridson, in *ACM SIGGRAPH 2007 Sketches* (ACM, San Diego, California, 2007), p. 22.

[91] C. Kamath, *Scientific Data Mining: A Practical Perspective* (SIAM, Philadelphia, 2009).

[92] M. A. Hall, *Correlation-Based Feature Selection for Discrete and Numeric Class Machine Learning* (Department of Computer Science, University of Waikato, Hamilton, New Zealand, 2000).

[93] L. Breiman, *Classification and Regression Trees* (Wadsworth International Group, Belmont, California, 1984).

[94] C. E. Rasmussen and C. K. I. Williams, *Gaussian Processes for Machine Learning* (MIT Press, Cambridge, Massachusetts, 2006).

[95] A. Okunkova, M. Volosova, P. Peretyagin, Y. Vladimirov, I. Zhirnov, and A. V. Gusarov, Phys. Proc. **56**(0), 48 (2014).

[96] A. Okunkova, P. Peretyagin, Y. Vladimirov, M. Volosova, R. Torrecillas, and S. V. Fedorov, Proc. SPIE **9135**, 913524 (2014).

[97] I. V. Zhirnov, P. A. Podrabinnik, A. A. Okunkova, and A. V. Gusarov, Mech. Ind. **16**, 709 (2015).

[98] A. Tarantola, *Inverse Problem Theory and Methods for Model Parameter Estimation* (SIAM, Philadelphia, 2005).